Master's thesis

NTNU
Norwegian University of Science and Technology
Faculty of Natural Sciences
Department of Physics

Sveinung Hansen Seltveit

Auroral Dunes: Bores or Boring?

Airglow Imaging of Gravity Wave-Aurora Interaction in the Mesosphere-Lower Thermosphere

Master's thesis in Applied Physics and Mathematics
Supervisor: Patrick Joseph Espy
Co-supervisor: Noora Partamies
June 2022

NTNU
Norwegian University of Science and Technology

UNIS
The University Centre in Svalbard

Sveinung Hansen Seltveit

Auroral Dunes: Bores or Boring?

Airglow Imaging of Gravity Wave-Aurora Interaction in the Mesosphere-Lower Thermosphere

Master's thesis in Applied Physics and Mathematics
Supervisor: Patrick Joseph Espy
Co-supervisor: Noora Partamies
June 2022

Norwegian University of Science and Technology
Faculty of Natural Sciences
Department of Physics

NTNU
Norwegian University of
Science and Technology

Acknowledgements

First and foremost, I would like to thank the dynamical duo that are my supervisors: Patrick J. Espy and Noora Partamies. Thanks to Patrick for giving me the opportunity to go to Svalbard, finding an intriguing project for me, as well as teaching me all I know about gravity waves, airglow and image processing. A huge *tusen takk* to Noora for welcoming me to Svalbard, always giving supersonic and helpful answers to questions and encouragement after many hours of unsuccessful airglow-watching. Also a thanks to the *KHO-troll* Mikko Syrjäsuo for helping out with projection and data collection.

Håvar and Maren, thank you for all the good times on and off campus at NTNU, with and without wine. Florina and Maria, thank you for making the time at Svalbard such fun with skiing, snowmobiling, rifle shooting and dinners. Also a thank you to the geophysics master student office at UNIS, for great company, lunch breaks and procrastination. Stein Kåre, thanks for the fun and competition through eight years of school, work and education together. To my parents, a big thank you for your support, even though you don't really know what I am doing. Finally, a big thank you to my girlfriend Ingvild for housing me at the finishing line, helping out when I needed it and all our nice trips together.

Abstract

Recently, a new auroral form named *dunes* was discovered using citizen scientist observations. The dunes were monochromatic, horizontal waves in the aurora and were observed in the mesosphere-lower thermosphere, which is a laboriously measured region of the atmosphere. Studies of dune events suggest that they are auroral manifestations of mesospheric bores, a rare type of atmospheric waves with characteristically high propagation speeds. In this thesis, all-sky airglow imaging is utilized to find and investigate auroral structures which resemble dunes. The structures resemble evenly spaced fingers, and the *finger structures* appear to have a connection to simultaneously observed gravity waves. Gravity waves are a type of atmospheric waves which occur more frequently than mesospheric bores. The principle goal of this thesis was to determine if the finger structures are gravity waves enhanced by the aurora, which supports that the dunes are an auroral manifestation of atmospheric waves, in addition to suggesting that ordinary gravity waves also can lead to dune structures.

Airglow data from Halley and Rothera research stations at Antarctica, and the Kjell Henriksen Observatory at Svalbard has been examined to find finger structure events. Three events were found in images of Na (sodium) and OH (hydroxyl) airglow from Halley taken in June 2000. Airglow images have been geographically projected, and auroral structures and airglow structures have been enhanced in respective images taken simultaneously. A connection between finger structures and gravity waves has been found for all three events. Finger structure separations and wavelengths of gravity waves have been estimated, compared and temporally analysed. Auroral influence on wavelengths was deemed to be low, indicating that the waves were no auroral phenomenon. Finger structure separations and wavelengths of gravity waves were found to be comparable for each event, indicating that the finger structures are gravity waves enhanced by aurora. Filtered OH airglow images was used to estimate wave propagation speeds for each finger structure event. The estimated speeds were in the range of 9.02-22.63 m/s, clearly indicating that the waves were gravity waves and not mesospheric bores.

Samandrag

Nyleg vart ei ny form av nordljos, kalla for *dyner*, oppdaga ved hjelp av observasjonar frå ei gruppe folkeforskarar. Dynene var monokromatiske, horisontale bylgjer i polarljoset, og vart observert i mesosfæren-nedre termosfæren, ein innfløkt del av atmosfæren å gjera målingar i. Studiar av dynehendingar føreslår at fenomenet er polarljosets manifestasjon i mesosfæriske tidevassbylgjer, ei svært sjeldan type atmosfæriske bylgjer med særmærkt høge fasesnøggleikar. I denne granskinga vert vidvinkelbilete av natthimmelljos nytta til å finne og granske strukturar i polarljos som har likskapar med dyner. Strukturane ser ut som jamt fordela fingrar, og desse *fingerstrukturane* verkar å ha ei kopling til samstundes observerte tyngdebylgjer. Tyngdebylgjer er ei type atmosfæriske bylgjer som førekjem langt oftare enn mesosfæriske tidevassbylgjer. Hovudmålet til denne granskinga var å var å fastsetje om fingerstrukturane var tyngdebylgjer som vart ljost opp av polarljoset, som stør at dynene er polarljosets manifestasjon av atmosfæriske bylgjer, i tillegg til at det føreslår at ordinære tyngdebylgjer også kan føre til dyneliknande strukturar.

Natthimmelljosdata frå forskningsstasjonane Halley og Rothera på Antarktis, samt Kjell Henriksen Observatoriet på Svalbard vart granska etter fingerstrukturhendingar. Tre hendingar vart funne i bilete av Na (natrium) og OH (hydroksyl) natthimmelljos frå Halley, tekne i juni 2000. Bileta vart geografisk projiserte, og polarljosstrukturar og natthimmelljosstrukturar vart forsterka i respektive, samstundes tekne bilete. Ein samanheng mellom fingerstrukturar og tyngdebylgjer vart funne for alle tre hendingar. Avstand mellom fingerstrukturar og bylgjelengder til tyngdebylgjer vart estimert og samanlikna. Deira tidsutvikling vart også analysert. Polarljosets påverknad på bylgjelengder vart fastsett til å vere låg, noko som tyder på at tyngdebylgjene ikkje var eit resultat av polarljoset. Avstandar mellom fingerstrukturar og bylgjelengdene til tyngdebylgjene var samanliknbare for alle hendingar, noko som tyder på at fingerstrukturane er tyngdebylgjer ljost opp av polarljoset. Filtrerte OH natthimmelljosbilete vart brukt til å estimere fasesnøggleikar til tyngdebylgjer for kvar fingerstrukturhending. Dei estimerte snøggleikane var imellom 9.02-22.63 m/s, som klart tyder på at bylgjene var tyngdebylgjer og ikkje mesosfæriske tidevassbylgjer.

Contents

List of Tables

List of Figures

List of Abbreviations

BAS British Antarctic Survey.

CCD Charge-Coupled Device.

EUV Extreme Ultraviolet.

FHWM Full Width at Half Haximum.

GWs Gravity Waves.

KHO Kjell Henriksen Observatory.

MLT Mesosphere-Lower Thermosphere.

UT Universal Time.

CHAPTER 1

Introduction

1.1 Background

Auroras are well known and spectacular luminous phenomena most frequently occurring in the polar regions (Egeland et al., 1973). The most elementary auroral forms are homogeneous arcs, bands, rays, patches and surfaces. On October 7th 2018, citizen scientists took several photographs of a new auroral form over Northern Europe named *dunes* (Palmroth et al., 2020). The new form, seen in figure 1.1, is a series of green stripes and unlike other known auroral forms. The dunes were determined to be a monochromatic wave field with a wavelength of 45 km propagating in a thin layer of diffuse aurora at 100 km altitude, in a region of the atmosphere called the Mesosphere-Lower Thermosphere (MLT). It was suggested that the wave field could be a mesospheric bore, a rarely detected type of atmospheric wave.

The 2020 dune event study furthermore reported six additional sightings, and in 2021 Grandin et al. studied another dune aurora event that was observed from Finland to Scotland on January 20th 2016. The horizontal wavelength of these dunes was found to be comparable to the 2018 event, with wavelengths in the range of 30-42 km. This study also estimated the propagation speed, which was around 200 m/s. Spacecraft observations indicated that the dunes were associated with particle precipitation and revealed the presence of a temperature inversion layer, which creates suitable conditions for mesospheric bores. Both Palmroth et al. and Grandin et al. suggested that the wave field is a mesospheric bore illuminated by aurora. There is also a possibility that the wave-like

structures are more directly connected to the aurora, e.g., that they somehow inherently are a part of the aurora, or that the aurora creates waves in the neutral atmosphere. Given that both the MLT and atmospheric waves are laboriously measured and modeled, understanding the mechanisms behind the dune structures may provide new insight into the drivers of climate and weather.

Figure 1.1: Dune event captured simultaneously in the aurora on October 7th 2018 over a) Latila and b) Ruovesi in Finland. The dune structures are marked by magenta circles and numbers. Reprinted from: Palmroth et al., 2020.

Atmospheric gravity waves (GWs) are similar to ocean waves at the interface between air and water, caused by the restoring effects of buoyancy and gravity. Originating in the lower atmosphere, they may propagate upwards to the MLT (Andrews, 2010). In 2003, Jarvis et al. described the utilization of an imaging riometer in combination with an airglow imager to study mesospheric GWs. Images from this event, obtained on June 7th 2000 on the British Antarctic Survey (BAS) Halley Research Station, show structures in the aurora that resemble dunes. See figure 1.2 for an airglow image depicting these structures. Already present GW structures simultaneously observed were seemingly con-

nected to the dune-resembling structures, hereby denoted *finger structures*. Although the previous mentioned dune studies point towards mesospheric bores, it is possible that GWs illuminated by aurora also appears as dune structures. Either way, finding a link between already present GWs and finger structures will support that the dunes are atmospheric waves illuminated by, and not created by or inherently a part of the aurora.

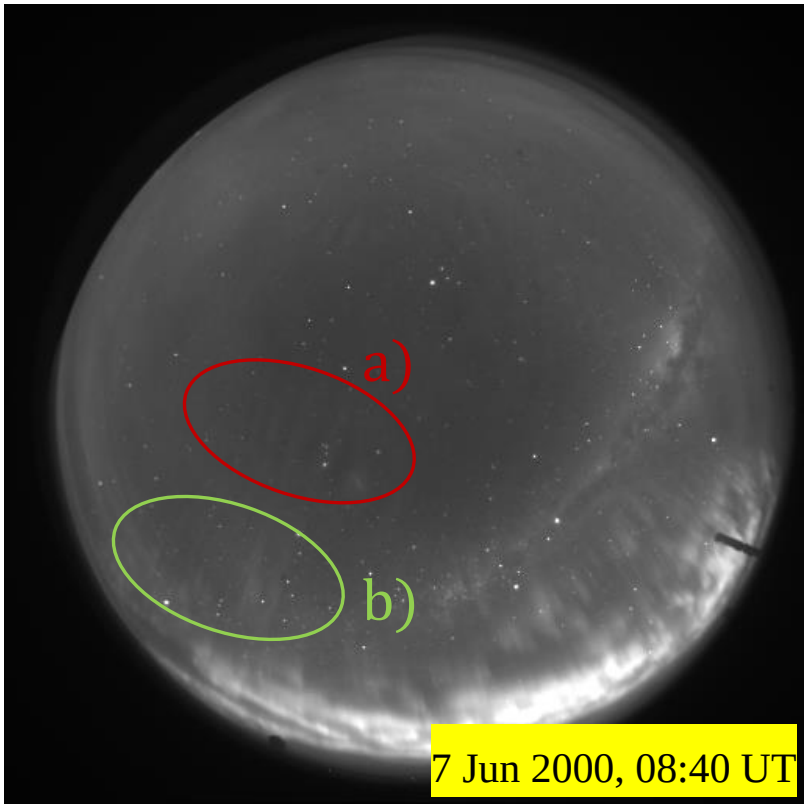

Figure 1.2: Raw, unprocessed airglow image from Halley Research Station taken at June 7th 2000, 08:40 UT (Universal Time). The image is taken with an OH filter. a) GWs circled out in red. b) Auroral structures resembling dunes circled out in green.

The focus area of this thesis is airglow data from the June 7th 2000 event, as well as finding other events with similar finger structures. The data examined for other events is airglow data from the BAS research stations at Halley and Rothera, in addition to airglow data from the Kjell Henriksen Observatory (KHO) at Svalbard. The aim is to locate and examine the connection between GW patterns and the finger structures in the aurora. If a connection is found, it suggests that the finger structures in fact are GWs illuminated by the aurora. A temporal analysis of wavelengths, as well as comparing these to corresponding parameters of the finger structures will also be of focus. A low auroral influence on wavelengths temporally, and a similarity between wavelengths and separation of finger structures will support a hypothesis that the finger structures are GWs illuminated by the aurora. Additionally, the wave speed will be of interest, given

that Palmroth et al. suggested that the dunes were mesospheric bores. Mesospheric bores and GWs have similar wavelengths, but the mesospheric bore speeds are characteristically high compared to GW speeds. Note that it will be assumed that all waves seen in the airglow data are GWs, given that they are a very common phenomena compared to the rare mesospheric bores. The waves will thus be called GWs until otherwise is indicated.

The thesis starts by giving the reader a basic, theoretic introduction to the MLT, GWs, spectroscopy, airglow, aurora and mesospheric bores. The basics of airglow imaging, specifications of airglow imagers used in the thesis work and image processing techniques are then presented. Subsequently, results are presented and discussed, before findings are summarised and further work is considered. Note that a preliminary study with a similar theoretic introduction and presentation of method was performed during the fall of 2021, causing this thesis and the report of the preliminary study to have alike introduction and method chapters.

1.2 The MLT

The section concerning the MLT is based on Plane, J.M.C.: *Atmospheric Chemistry of Meteoric Metals* (Plane, 2003).

The atmosphere is divided into layers defined by their vertical temperature profiles, as seen in figure 1.3. The region extending from 75 to 110 km altitude is referred to as the MLT, and is of particular interest since it forms the boundary between the atmosphere and space. The region is majorly influenced by high energy inputs from above by solar radiation and solar winds, as well as below by atmospheric waves and tides. Given that the dune structures were found in the MLT, it is the region of interest for the thesis work.

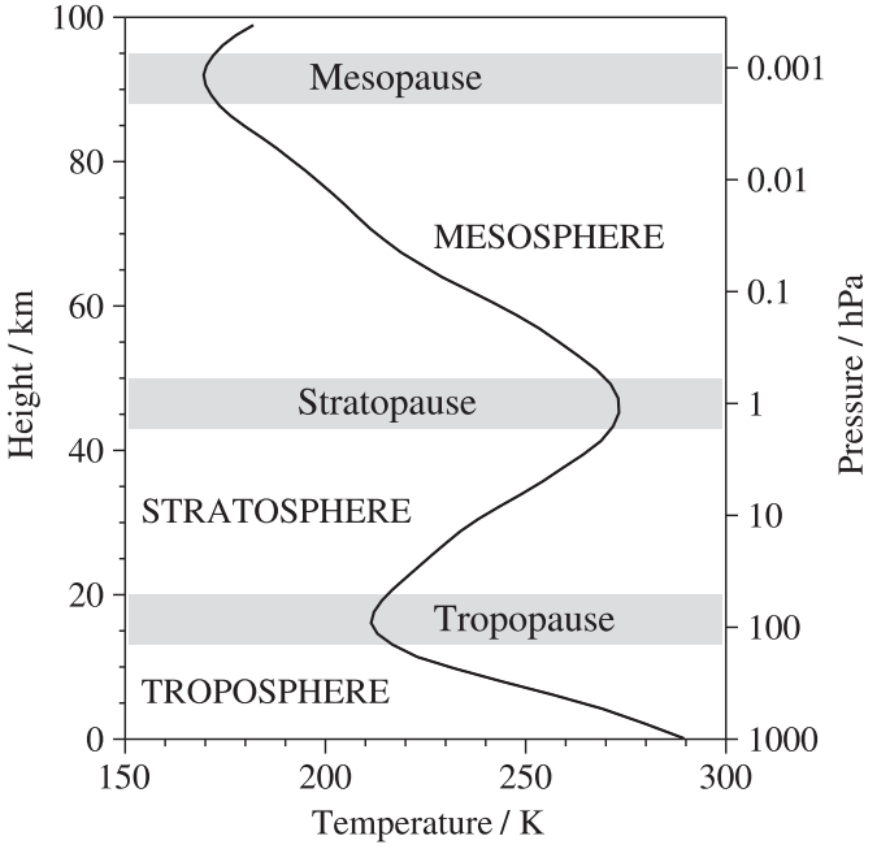

Figure 1.3: Typical vertical atmospheric temperature and pressure profile. Atmospheric regions are labelled with capital letters, while the boundaries between them are shaded. Reprinted from *An Introduction to Atmospheric Physics.*, D.G. Andrews, 2010.

The mesosphere begins at the stratopause around 50 km altitude. Throughout the mesosphere, temperature decreases from a local maximum in the stratopause to a minimum at the mesopause. The mesopause is the coldest part of the atmosphere, and is

found between 85-100 km altitude depending on season. The thermosphere begins over the mesopause, where extreme ultraviolet (EUV) and X-ray radiation causes temperature to rise with altitude. Temperatures reach 1000 K in the thermosphere, but are mostly kinetic due to low density. The high EUV absorption of the thermosphere causes local heating in the mesosphere to be low. This is a major contributor to the low temperature of the mesosphere, along with low pressure, which causes greenhouse gases to act as infrared radiators, cooling the MLT region.

Opposed to the lower parts of the atmosphere, which are coldest in the winter, the MLT is coldest in the summer. GWs, presented in section 1.3, are the cause of this phenomenon. GWs originating in the troposphere transport large amounts of energy, which is deposited in the MLT region. The deposited energy leads to a drag on the zonal wind, causing a equatorward meridional flow. The upwelling air at high latitudes which feeds the flow is cooled by adiabatic expansion, leading to temperatures as low as 120 K. If the summer mesopause were to be in thermal equilibrium at high latitudes it would have a temperature of around 220 K.

The low pressure of the MLT not only affects its temperature. It also causes the mean free path of air molecules to approach 1 m at 110 km altitude. This leads to diffusion being dominant, as bulk motion of the air cannot be sustained. Another consequence is that atomic oxygen is the major reactive species in this region. Atomic oxygen is removed by recombining reaction between O and O_2, which forms O_3. At heights above 82 km, the time constant for O-removal exceeds 12 hours, causing an active radical chemistry to continue throughout the night.

1.3 Gravity Waves

The section concerning gravity waves is based on Andrews, D.G.: *An Introduction to Atmospheric Physics* (Andrews, 2010, pp. 3, 12-13, 128-132), and inspired by a lecture given by Patrick Espy (2021).

An important feature of the buoyancy restoring effect in a stably stratified atmosphere is that it can support fluid-dynamical waves known as atmospheric GWs. They are analogous to the horizontally propagating surface waves on water, which depend on the restoring mechanism provided by the density difference between air and water. GWs are generated in many manners, including convective activity in the troposphere and airflow over mountains. They play an essential role in the global circulation of the atmosphere, transporting large amounts of energy and momentum from the troposphere to the MLT.

As mentioned in section 1.2, GWs influence both the spatial and temporal characteristics of this region.

1.3.1 The Air Parcel

In order to explain the origin of GWs, the concept of an air parcel is introduced. An air parcel is a mass of air that is influenced by the environment, while itself cannot change the environment. The parcel pressure is identical to its surroundings, but its temperature, density and composition may differ from those of the environment. The air parcel can be imagined as a mass of air confined to a thin, mass-and-surface tensionless balloon that rises and falls adiabatically in a hydrostatic atmosphere. Figure 1.4 illustrates an air parcel as it rises adiabatically from an altitude z_0 to $z_0 + \delta z$:

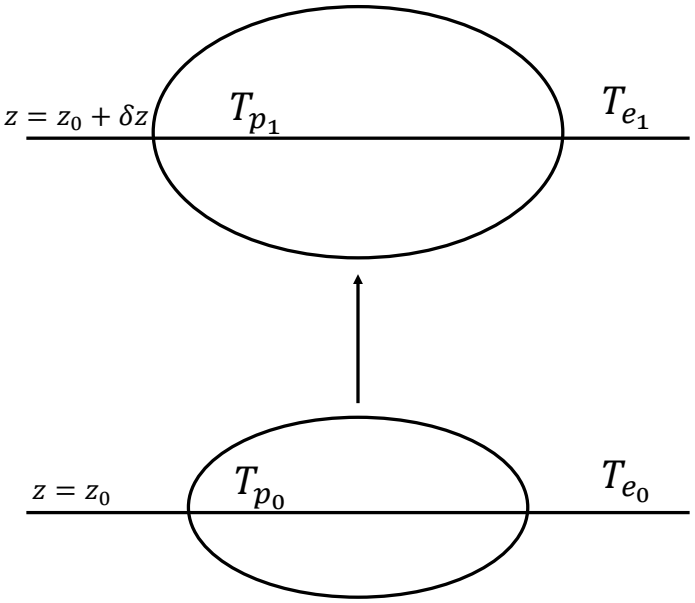

Figure 1.4: An air parcel rising adiabatically in the atmosphere from height $z = z_0$ to $z = z_0 + \delta z$, changing its temperature from T_{p_0} to T_{p_1} because of the pressure decrease. Since the parcel pressure is identical to its surroundings, the parcel volume increases. Atmospheric temperature is denoted T_{e_0} and T_{e_1}, and may be different at the two heights. Adapted from *An Introduction to Atmospheric Physics.*, D.G. Andrews, 2010.

Since the parcel rises adiabatically, its temperature decrease is given by:

$$-\left(\frac{dT_p}{dz}\right) = \frac{g}{c_p} \equiv \Gamma_a, \tag{1.1}$$

where g is the gravitational acceleration and c_p is the specific heat capacity of air at constant pressure. The adiabatic temperature decrease is denoted as $\Gamma_a \approx 9.8$ K/km. The temperature decrease of the atmosphere can in the same manner be defined as $\Gamma = -(dT_e/dz)$, and is generally not constant with altitude, as seen in figure 1.3. Examining the case of the rising parcel in figure 1.4, the parcel temperature and atmospheric temperature will respectively be given by:

$$T_{p_1} = T_{p_0} - \Gamma_a \delta z \tag{1.2}$$

$$T_{e_1} = T_{e_0} - \Gamma \delta z, \tag{1.3}$$

at altitude $z = z_0 + \delta z$. The following expressions for parcel and atmospheric density can be obtained using the ideal gas law and equations 1.2 and 1.3:

$$\rho_{p1} = \frac{p_1}{R_a T_{p1}}, \quad \rho_{e1} = \frac{p_1}{R_a T_{e1}}. \tag{1.4}$$

As the volume of the parcel at height $z_0+\delta z$ is equal to the volume of the air it displaces, the parcel will be heavier than the air it displaces if $\rho_{p1} > \rho_{e1}$. From equation 1.4, this is the case if the parcel is colder than the atmosphere, i.e. $\Gamma_a > \Gamma$. In this case, the parcel will fall back to its equilibrium position due to gravity, and an atmosphere behaving like this is characterised as stable. On the other hand, if $\Gamma_a < \Gamma$, the atmosphere is characterised as unstable, as an upward displaced parcel will be lighter than its surroundings and continue to rise.

1.3.2 Propagation

The key forces behind a GW are gravity and buoyancy. The upward buoyancy force for an upward displaced air parcel at height $z + \delta z$ is given by:

$$F_b = g V_1 (\rho_{e1} - \rho_{p1}), \tag{1.5}$$

where V_1 is the volume of the parcel at this height. By Newton's second law, the force may also be written as:

$$\sum_i F_i = F_b = \rho_{p1} V_1 \frac{d^2(\delta z)}{dt^2} \tag{1.6}$$

This leads to:

$$\begin{aligned}\frac{d^2(\delta z)}{dt^2} &= g\big(\frac{\rho_{e1}}{\rho_{p1}} - 1\big) = g\big(\frac{T_{p1}}{T_{e1}} - 1\big) \\ &= g\big(\frac{T - \Gamma_a \delta z}{T - \Gamma \delta z} - 1\big) = g\big(\frac{\Gamma - \Gamma_a}{T - \Gamma \delta z}\big)\delta z \\ &= -\frac{g}{T}(\Gamma_a - \Gamma)\delta z,\end{aligned} \tag{1.7}$$

to leading order in δz and using equation 1.4 to get the third expression. Examining equation 1.7, it is apparent that it is an equation of the form:

$$\frac{d^2(\delta z)}{dt^2} + N^2(\delta z) = 0, \quad N^2 = \frac{g}{T}(\Gamma_a - \Gamma). \tag{1.8}$$

In the case where $N^2 > 0$, i.e. $\Gamma_a > \Gamma$, the equation describes simple harmonic motion with sinusoidal solutions. In the other case, where $N^2 < 0$, i.e. $\Gamma_a < \Gamma$, the equation has exponential solutions. The quantity N is called the buoyancy frequency or the Brunt-Väisälä frequency. Note that the solutions of 1.8 are consistent with the concept of atmospheric stability.

If the displacement of an air parcel is purely vertical, GWs will not propagate, since the air simply oscillates around an equilibrium point. In order to have a vertically and horizontally propagating GW, a vertical and horizontal displacement is necessary. For the sake of visualisation, envisioning a corrugated sheet moving through air is beneficial, illustrated by figure 1.5. The sheet pushes the air upwards and forwards at point A. The push propagates, causing the gray region to have an increased pressure with air that rises, expands and cools. At the point B on the other hand, the sheet pulls the air downwards and backwards. The pull will also propagate, causing the region of the broken grey lines to have a decreased pressure with air that falls, compresses and heats. The energy propagation will move upwards and forwards, transporting energy vertically.

As a GW propagates upwards in the density-decreasing atmosphere, its amplitude grows with height in order to conserve energy and momentum. Eventually, the wave becomes non-linear and unstable, depositing its energy and momentum locally, analogous to whitecaps in a breaking ocean wave. GWs may also break and deposit energy if they encounter an unstable region of the atmosphere, or if they reach a region in which the background winds exceed the horizontal phase velocity of the wave (Espy, 2021).

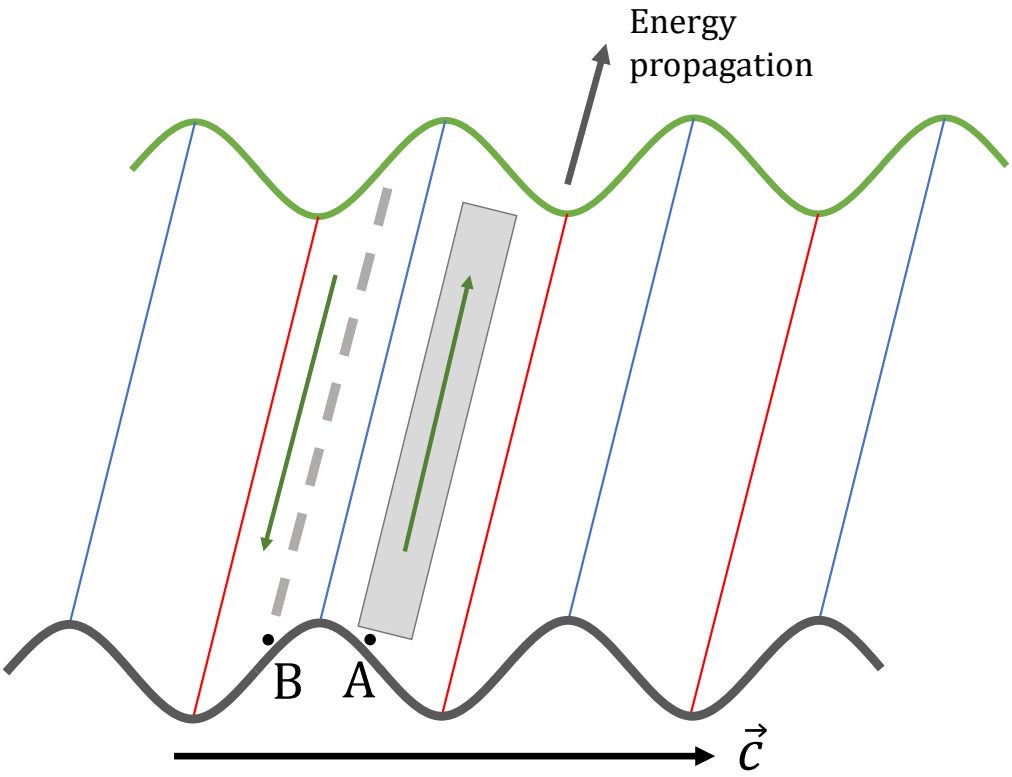

Figure 1.5: A corrugated sheet (black line) moving through air with velocity $\vec{c}$. The air at A and in the gray region will rise and cool, while the air at B and in the region of the dashed gray line will fall and heat. Energy propagates upwards. Adapted from a figure by W.H. Hocking: Personal communication, 2001.

1.3.3 Mathematical Modeling

In order to improve the understanding of GWs, mathematical modeling is useful. Starting with the Navier-Stokes equations, ideal gas law and hydrostatic equation, one can come to the Boussinesq equations by neglecting the compressibility effects in the atmosphere. Thereafter, the equations may be linearized by assuming small velocity and density deviations. These equations are called the linearized Boussinesq equations:

$$\begin{aligned} u_t - fv + \frac{1}{\rho_0} p'_x &= 0, \\ v_t + fu + \frac{1}{\rho_0} p'_y &= 0, \\ u_x + v_y + w_z &= 0, \\ -\frac{g}{\rho_0}\rho'_t + N^2 w &= 0, \\ p'_z + g\rho' &= 0. \end{aligned} \tag{1.9}$$

In equations 1.9, a subscript denotes a partial derivative with respect to the subscripted quantity. u, v and w are velocities in x, y and z-directions respectively. ρ is the density, ρ_0 is a reference density, g is the gravitational acceleration, N is the buoyancy frequency, p is pressure and f is a Coriolis-force term. GWs propagate upwards and forwards, so plane wave solutions in the x, z-plane that are independent of y-direction are inserted. It can then be shown that the dispersion relation for internal GWs is given by:

$$\omega^2 = \frac{N^2 k^2}{m^2} \iff \omega = \pm \frac{Nk}{m}. \tag{1.10}$$

ω is the angular frequency, and k and m are the wave numbers in x-,and z direction respectively. Determining which of the two solutions that represent an upward-propagating GW can be done by examining the group velocity:

$$\vec{c_g} = (c_{g_x}, 0, c_{g_z}) = (\frac{\partial \omega}{\partial k}, 0, \frac{\partial \omega}{\partial m}) \tag{1.11}$$

Inserting equation 1.10 into equation 1.11, the vertical group velocity is found to be:

$$c_{g_z} = \mp \frac{Nk}{m^2}. \tag{1.12}$$

For an upward propagating GW, we have $c_{g_z} > 0$, and the correct solution for the angular velocity is thus given by:

$$\omega = -\frac{Nk}{m}. \tag{1.13}$$

Several features can be noted from this. First of all, the phase surfaces $kx + mz - \omega t =$constant move obliquely downwards in time, in the direction of the wave vector $\vec{k}$. The propagation of information however, represented by the group velocity $\vec{c_g}$ is obliquely upwards. Furthermore, the velocity vector $(u, 0, w)$ is parallel to the slanting phase surfaces, parcels oscillate up and down these surfaces. Figure 1.6 illustrates the cross section of a plane internal GW propagating upwards.

Normally, horizontal wavelengths are much larger than vertical wavelengths. Therefore GWs normally have an angular frequency which is much smaller than the buoyancy frequency:

$$\lambda_H >> \lambda_V \implies k^2 << m^2 \implies \omega^2 << N^2. \tag{1.14}$$

Even for non-hydrostatic waves, it turns out that $\omega^2 \leq N^2$, giving typical minimum periods $T_{min} = 2\pi/N$ of 8 minutes for the troposphere and 5 minutes for the stratosphere and MLT for GWs. It should be noted that these results are derived for a class of GWs whose horizontal scales are so small that the Earth's rotation can be neglected. This needs

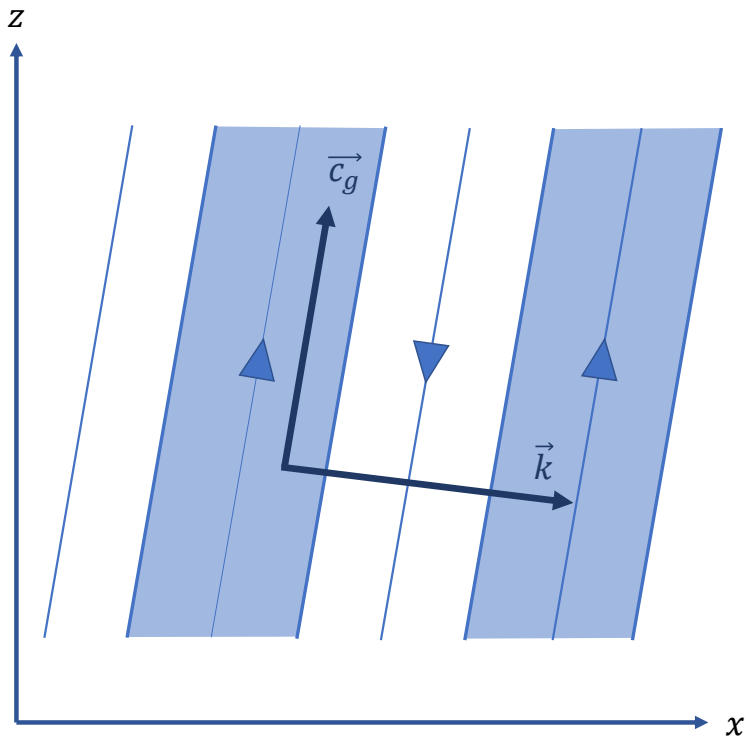

Figure 1.6: Vertical cross section of a GW propagating upwards with upward pointing group velocity $\vec{c_g}$ and downward pointing wave vector $\vec{k}$. The thin sloping lines represent surfaces of constant phase, separated by a quarter wavelength. The surfaces on which the pressure and density disturbances take their greatest absolute values are marked by triangles. Regions of upward motion are shaded, and the phase surfaces move perpendicular to themselves as time progresses. Adapted from *An Introduction to Atmospheric Physics.*, D.G. Andrews, 2010.

to be accounted for when considering larger-scale waves with periods of several hours.

1.4 Basic Spectroscopy

The following section is based on Hemmer, P.C.: *Kvantemekanikk* (Hemmer, 2005, p. 195) and Andrews, D.G.: *An Introduction to Atmospheric Physics* (Andrews, 2010, pp. 63-66).

Spectroscopy of atoms and molecules are key principles in observation of both aurora and airglow. The basics of this is hence presented.

Atoms and molecules do not take continuous energy levels, only certain discrete levels. The possible energy levels are determined by the quantum mechanical state of the system. A natural starting point is the hydrogen atom. A simplified quantum mechanical model

of the Coulomb-potential gives the following energy levels:

$$E_i = -\frac{m}{2\hbar^2}\Big(\frac{e^2}{4\pi\epsilon_0}\Big)^2\frac{1}{n_i^2}, \tag{1.15}$$

where $n_i = 1, 2, ...$ is the quantum number characterising the electronic energy level, $m = m_e m_p/(m_p + m_e)$ is the reduced mass of the system, $\hbar$ is Planck's reduced constant, e is the elementary charge and ϵ_0 is the vacuum permittivity. An energy of zero is equivalent of complete separation between proton and electron. If energy is added to the system, it is excited to a higher energy state E_f, $n_f = 1, 2, ...$ and $n_i < n_f$ In order to lose its excess energy, the system can de-excite by emitting a photon with energy equal to the difference between the energy levels:

$$h\nu = E_i - E_f = \frac{m}{2\hbar^2}\Big(\frac{e^2}{4\pi\epsilon_0}\Big)^2\Big(\frac{1}{n_f^2} - \frac{1}{n_i^2}\Big), \tag{1.16}$$

where h is Planck's constant and ν is the wavelength of the photon emitted. A limitation is imposed on possible energy transitions by the angular momentum of the electron, which also takes discrete levels $L = \sqrt{l(l+1)}\hbar$, where $l = 0, 1, .., n-1$, is the angular momentum quantum number. Allowed transitions have $\Delta l = \pm 1$. The quantisation of energy and limitation imposed on transitions causes the atom to emit light at certain discrete wavelengths, denoted emission lines. Atomic energy levels and excitation are more complicated in the general case, but the principles presented for the hydrogen atom do however provide a qualitative overview of the mechanisms involved.

Determining the diatomic molecular energy levels is far less trivial than the atomic case. In addition to the electronic energy, both the vibrational and rotational energy of the molecule must be accounted for. These energies are furthermore quantised, and the total energy can be split into electronic, vibrational and rotational energies:

$$E_{tot} = E_e + E_v + E_r \tag{1.17}$$

Beginning with the vibrational energy, the molecule can be approximated as a harmonic oscillator, which quantum mechanically has energy levels:

$$E_v = hv_0(v + 1/2), \tag{1.18}$$

where $v = 0, 1, ...$ is a vibrational quantum number, and v_o is the frequency of the harmonic oscillator. The energy-levels of the quantum mechanical harmonic oscillator are non-degenerate. Additionally, the energy will depend on the inter-nuclear separation similarly

to a parabola converging towards a critical inter-nuclear separation r_c where the atoms separate.

The rotational energy will also be quantised:

$$E_J = \frac{1}{2I} J(J+1)\hbar^2, \tag{1.19}$$

where I is the molecular moment of inertia and $J = 0, 1, ..$ is a rotational quantum number. The rotational energy levels are degenerate, with $2J + 1$ states corresponding to each energy value E_J. Similarly as for energy level transitions in the hydrogen atom, several rules apply to which transitions are allowed in a diatomic molecule. The addition of vibrational and rotational energy levels leads to a splitting of electronic energy levels. The limitations and splitting cause photons to be emitted in bands associated with vibrational levels, denoted emission bands. The bands consist of rotational energy levels. A naive illustration of the energy levels in a diatomic molecule is given in figure 1.7.

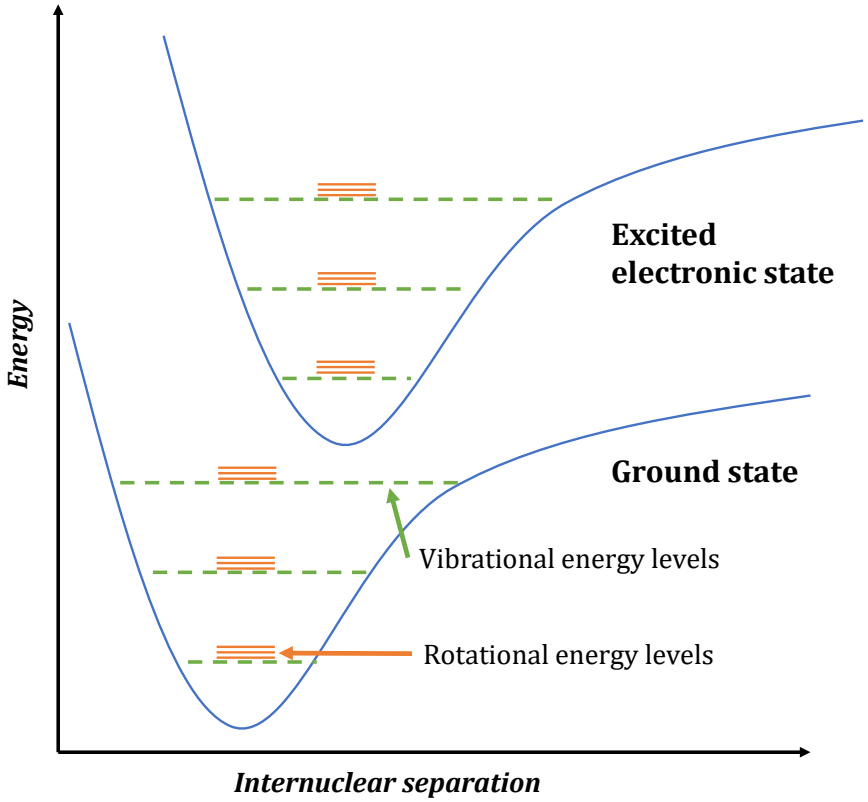

Figure 1.7: Illustration of the energy levels in a diatomic molecule for a ground electronic state and an excited electronic state. The continuous curved lines represent potential energy as a function of inter-nuclear separation. Dashed lines represent vibrational energy levels, and the small, solid lines represent rotational energy levels, forming emission bands. Adapted from *An Introduction to Atmospheric Physics.*, D.G. Andrews, 2010.

1.5 Airglow

Airglow is the emission of photons from atmospheric constituents excited in a direct or indirect way by electromagnetic radiation from the sun (Egeland et.al., 1973, p. 81). Examples of direct excitations are resonance radiation of alkali metals, while examples of indirect excitations are associated with the recombination of ionised or dissociated particles produced by the UV absorption of sunlight during the day. Airglow emissions come from layers in the atmosphere, characterised by their emission wavelength and emitting species. Several layers peak in the MLT region, causing airglow measurement to be an efficient ground-based observation method of this region of the atmosphere. Figure 1.8 shows an illustration of the intensity of different layers as a function of altitude. The emission layers examined in this thesis work are the sodium (Na) and hydroxyl (OH) layers, both produced by the recombination of dissociated particles. In order to give the reader an understanding of the basic principles behind these, a brief presentation of their chemistry and structure is given.

1.5.1 Na Airglow

The atmospheric Na layer was discovered by Vesto Melvin Slipher in 1929, observing radiation at 589 nm in the night sky spectrum. It was later identified as airglow emission from neutral sodium atoms (Bernard, 1939). The neutral and ionic forms of sodium that form the MLT Na layer extends from 80 to 110 km altitude, peaking at around 90 km. The major source of Na species in the MLT is meteor ablation (Plane, 2003). The chemical scheme that excites neutral Na atoms in the atmosphere was proposed by Chapman in 1939:

$$\mathrm{Na} + \mathrm{O_3} \xrightarrow{k_1} \mathrm{NaO} + \mathrm{O_2} \tag{1.20}$$

$$\mathrm{NaO} + \mathrm{O} \xrightarrow{\alpha k_2} \mathrm{Na^*(^2P_J)} + \mathrm{O_2} \tag{1.21}$$

$$\xrightarrow{(1-\alpha)k_2} \mathrm{Na(^2S)} + \mathrm{O_2}$$

$$\mathrm{Na^*(^2P_J)} \longrightarrow \mathrm{Na(^2S)} + \mathrm{h}\nu \ (589,\ 589.6\,\mathrm{nm}) \tag{1.22}$$

where k_i are respective rate coefficients and α is the branching ratio of reaction 1.21. The asterisk hereby denotes an excited species, and $(^{2s+1}L_J)$ represents the term symbol of the atom. s denotes the total spin quantum number, L denotes the total orbital quantum number in spectroscopic notation and J denotes the total angular momentum quantum number. The term $\mathrm{h}\nu(\lambda)$ represents emitted photons and their wavelengths. λ=589 nm and λ=589.6 nm correspond to radiation from J=3/2 and J=1/2 respectively.

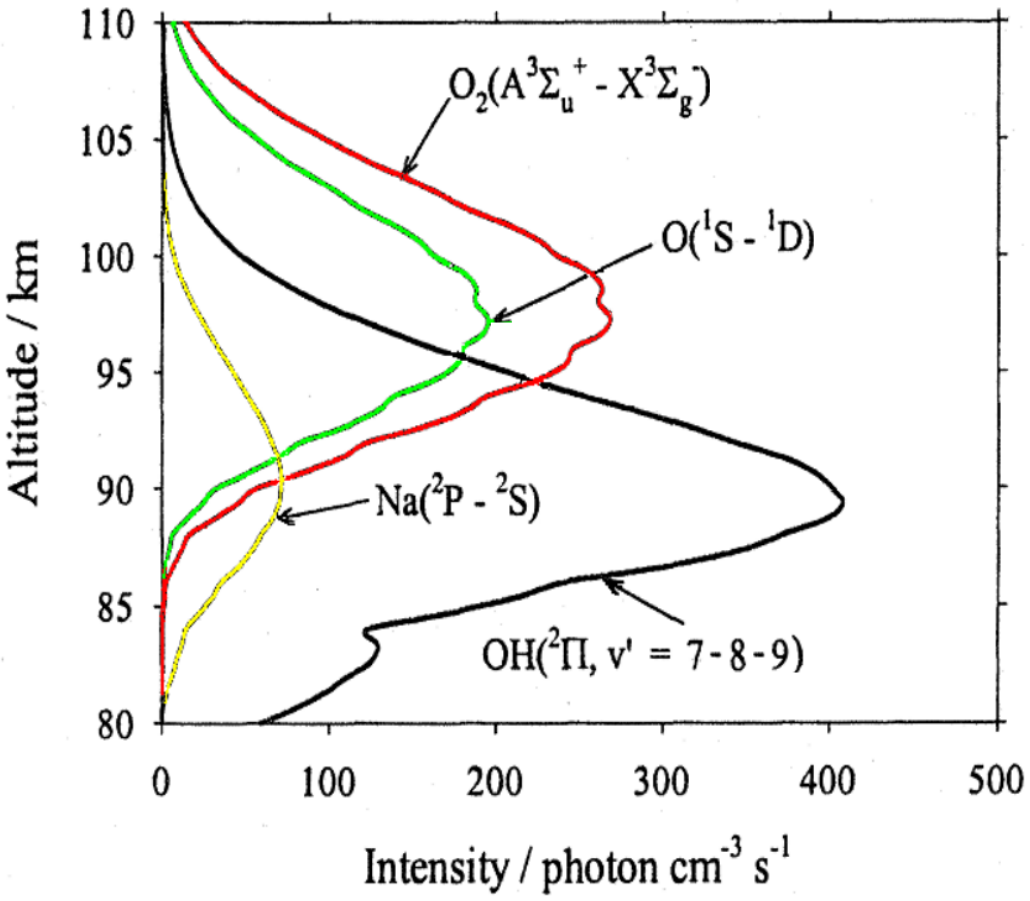

Figure 1.8: Modeled vertical intensity profiles (in photons/cm^{-3}s^{-1}) of different airglow emission layers. Each layer is labelled by its emitting species. Note that these are modeled, and that the figure only illustrate the differences between different airglow layers. Reprinted from J. Plane: Personal communication.

1.5.2 OH Airglow

OH is a diatomic molecule, meaning its airglow emission spectrum will consist of emission bands, cf. section 1.4. The emissions were discovered by Meinel in 1950. The OH layer peaks between 80 and 90 km altitude, and is mainly produced by the reaction (Bates & Nicolet, 1950):

$$\mathrm{H} + \mathrm{O_3} \xrightarrow{k_H} \mathrm{O_2} + \mathrm{OH}^*(\nu' \leq 9), \tag{1.23}$$

where k_H is the rate coefficient and ν' denotes the vibrational level of the molecule. Up to half of the OH* observed in the winter mesopause over Svalbard is further produced by the reaction (Sivjee & Hamwey, 1987):

$$\mathrm{HO_2} + \mathrm{O} \xrightarrow{k_H} \mathrm{O_2} + \mathrm{OH}^*(\nu' \leq 6). \tag{1.24}$$

Airglow spectroscopic observations reveal OH bands originating from $\nu' = 1$ to 9, and it has been shown in laboratory investigations that reaction 1.23 produces OH^* with $\nu' = 6, 7, 8, 9$ (Charters et al., 1971). The lower vibrational levels are produced as the excited molecule decreases its energy by rotational and vibrational transitions. There are several OH emission bands, with emission wavelengths ranging between 400 and 4000 nm. At KHO, the emission band formed by the transition $\nu' = 6$ to $\nu' = 2$ (6-2 Meinel band) is imaged, while several near infrared emission bands over the wavelength range of 715 to 950 nm are imaged at Halley and Rothera.

1.6 Aurora

The section on aurora is based on Egeland et al.: *Cosmical Geophysics* (Egeland et al., 1973, pp. 33-35, 121-123, 172-173, 203-205, 222-223.)

Aurora, named Aurora Borealis in the north and Aurora Australis in the south, is a light emission phenomenon. It happens most frequently in latitudinal belts roughly 23° from the geomagnetic poles, named the auroral zones. In the northern hemisphere it is located over the northern parts of Siberia, Alaska, Canada and the Nordics, while it in the southern hemisphere is located around Antarctica. Aurora may occur both closer and further from the poles, depending on the geomagnetic activity, described by the planetary-K index K_p. The visible auroral spectrum consists of several spectral lines and bands ranging from the ultraviolet to the infrared. Measurements by Størmer (1955) showed that the auroral arcs and bands mostly lie within the height interval of 90-150 km, although longer rays may stretch up to several hundred km in the atmosphere.

The aurora is produced by the interaction between solar winds, electrically charged particles from the Sun, and the Earth's magnetic field. The solar wind, consisting of both positively and negatively charged particles, is emitted at high velocities nearly radial from the sun. The solar wind can reach velocities of over 700 km/s, but is on average around 400 km/s. The solar wind particles are electrically charged, and will thus experience a force entering the Earth's magnetic field:

$$\vec{F_B} = q(\vec{v} \times \vec{B}), \tag{1.25}$$

where q is the charge of a particle, $\vec{v}$ is its velocity and $\vec{B}$ describes the magnetic field.

Decomposing the force into components that are parallel and perpendicular to $\vec{B}$, the parallel component can be shown to be $F_{B||} = 0$. The perpendicular component, $F_{B\perp}$ will

describe a circular gyration where the centrifugal force balances $\vec{F_B}$. The particles will travel in spiral-formed trajectories along the magnetic field lines, guiding the particles towards the polar areas. As the charged particles move downwards, the density of the surrounding atmosphere grows, and most of their energy is transferred to atmospheric atoms and molecules by collisions. Some of the transferred energy excites these atoms and molecules, leaving them in an excited energy state. These subsequently de-excite by emitting photons, which are the auroral emissions. Some of most prominent emissions are due to molecular nitrogen and atomic oxygen. It should be noted that the explanation of aurora given only describes the so-called day-side aurora, in which aurora happens at the side of Earth directly facing the sun. For the so-called night-side aurora, which happens at the side of Earth facing away from the sun, solar wind particles are stored and accelerated in the magnetosphere. Then, they enter the atmosphere at the night-side, after which they excite atmospheric particles as described for day-side aurora.

1.7 The Rayleigh

In order to give the reader an understanding of how airglow emissions and aurora compare in terms of intensity, the Rayleigh is introduced. It is a unit originally introduced as a measure for the total column light emission rate from optically thin gas species in the upper atmosphere (Hunten et al., 1956). It was further suggested to be used as a unit for surface brightness by Chamberlain (1961), after which it has been adopted by experimentalists in aeronomy (Baker & Romick, 1976). Historically, it was defined as a column emission rate of 10^{10} photons per square meter per column per second:

$$1\ \mathrm{R} \triangleq 10^{10}\ \text{photons}\ \ \sec^{-1}\ (\mathrm{m}^2 \cdot\ \mathrm{col})^{-1}, \tag{1.26}$$

but it has also been defined as a unit for apparent photon radiance, $1\ \mathrm{R} \triangleq 1/4\pi\, 10^{10}$ photons $\sec^{-1}\mathrm{m}^{-2}\mathrm{sr}^{-1}$. Using the first definition, the Rayleigh is a useful unit for measuring and comparing the emission rates of both airglow and aurora, as both are light emissions associated with the excitation of atmospheric constituents. Note that the analysis in this thesis work is done on uncalibrated data given in pixel brightness. Emission rates, given in kR, both for the aurora and different airglow layers examined in this project are given in table 1.1:

Table 1.1: Emission rates given in kR for aurora and different airglow layers. OH value is an estimated total. Values adapted from *The Rayleigh: A Photometric Unit for the Aurora and Airglow.* J.W. Chamberlain, 1995.

Source	Emission rate (kR)
Aurora	1-1000
Na night airglow	0.03-0.2
O_2 night airglow	1.5
OH night airglow (total)	4500

1.8 Mesospheric Bores

Mesospheric are rare wave events identified by several specific characteristics. The first event sighted and suggested to be a mesospheric bore happened in 1993 (Taylor et al., 1995). It was characterised by a sharp leading front, followed by a series of wave crests with the same velocity as the front. The front and the waves showed a 180° phase reversal observed in the OH airglow layer and the O airglow layer, which peaks at a higher altitude than the OH airglow layer. The front was characterised by a sudden increase in OH airglow intensity, and a coincidental decrease in the O airglow intensity. Similarly, the wave appeared as a bright wave propagating through a dark sky in the OH-emissions, while it appeared as dark wave propagating through a bright sky in the O-emission. The wave motion exhibited a horizontal wavelength of λ_H=19.3 km, and an apparent phase speed c=76 m/s.

In 1998, Dewan & Picard suggested that this intriguing event showed the characteristics of a mesospheric bore. Whilst bores are rarely detected in the upper mesosphere, they are a well-known phenomena that often occurs in shallow seas, river estuaries and in the troposphere. Dewan & Picard developed a simple two-layer model for bore propagation analogous to the theory of bores in river channels. For the bore case concerning water in river channels, it forms when tidal water flows up a river. The bore is the front formed between the in-flowing tidal water, and the support and stability of the channel bottom allow waves to form. The waves carry away the energy loss due to difference of work between the two sides of the bore, and are highly unstable. Dewan & Picard further present the thermocline bore case, where a bore propagates in a stable region in the upper ocean, with regions of reduced stability above and below. The thermocline bore can oscillate in a mode where the upper and lower surfaces of the bore oscillate 180 ° out of phase, similarly to the event reported by Taylor et al. in 1995. It is thus argued that a region of high stability in the atmosphere, surrounded by regions of lower stability could form a guiding channel comparable to the thermocline bore channel. Such a bore was named a symmetric undular bore, which oscillates around a symmetrical plane S. It

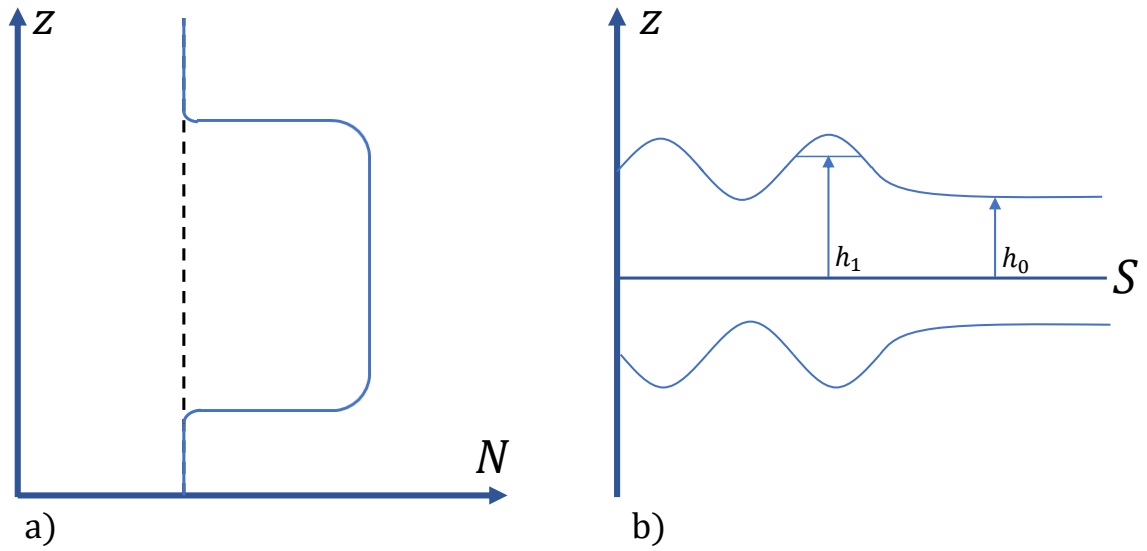

Figure 1.9: a) The buoyancy frequency N as a function of altitude z for a bore-guiding channel. b) Depiction of a symmetrical undular bore with symmetry plane S. Bore of height h_1 moving in channel with height h_0. Note that the figures are only meant as illustrations. Reprinted from: Dewan & Picard, 1998.

was suggested that a sudden heating event could give arise to such a channel. See figures 1.9 for an illustration of a guiding channel and a symmetric undular bore. Even though Dewan & Picard's model used a simplified representation of the guiding channel, their results were in agreement with the observations from the event in 1993, supporting that it was a mesospheric bore.

In 2001, Nielsen et al. presented a climatological study of mesospheric, short-period GW events observed over Halley Research Station. Observations were made during the 2000 and 2001 winter seasons, using data from the airglow imager also used in this thesis. Wave parameter distributions were found to be similar to those at other latitudes. The majority of the waves were found to have horizontal wavelengths (λ_H) in the range 15-40 km, with a mean value of around 26 km. Typical phase speeds (c_p) were found to be in the range 30-60 m/s, with an average value of around 48 m/s. The 1993 event in comparison thus has a typical wavelength, but a rather high phase speed. In 2005, Nielsen et al. studied a mesospheric bore event from Halley at May 27th 2001. The bore had wavelengths in the range of 18-31 km and a phase speed in the range of 64-78 m/s, with decreasing velocities and wavelengths throughout the event. If a wave observed in the thesis work should be deemed a mesospheric bore, it should thus at least have an observed speed of 64 m/s. It is also worth noting that both the 1993 and 2001 mesospheric bore events have wavelengths considered typical considering the Nielsen et al. climatology study.

CHAPTER 2

Method

The data used in the thesis work is as mentioned all-sky airglow images from Halley Research Station (76°S, 27°W) and Rothera Research Station (67°S, 68°W) at the Antarctic continent, in addition to airglow images from KHO (78°N, 16°E) at the Svalbard archipelago. Airglow images of the sky are taken with narrowband filters, which only transmit certain spectral bands or lines. Since a GW propagation perturbs the density of the region in which it propagates, airglow images will reveal GW structures. Both the BAS imager, which was used at both Halley and Rothera, and the KHO imager have filters that are affected by the aurora to different extents. This section presents the basics of airglow imagers, as well as image processing and analysis techniques, which have been performed in MATLAB R2020b (MATLAB, 2020).

2.1 Airglow Imager

The description of the airglow imagers is based on Taylor, M.: *The Utah-BAS Airglow Imaging Experiment Operation Manual* (Taylor, 2000), Espy, P.: Personal Communication (Espy, 2021) and Partamies, N.: Personal Communication (Partamies, 2022).

The aperture of an airglow imager consists of an all-sky lens with a 180° angle of view, a telecentric lens system, a narrowband interference filter wheel, an optical tube with a re-imaging lens, and a Charge-Coupled Device (CCD) detector. Figure 2.1 shows a schematic of an imager. Narrowband interference filters permit the isolation of wavelength intervals of a few nanometers or less in width, thus being highly effective in measurements of airglow layers. A simple portrayal of a narrowband interference filter is two coated

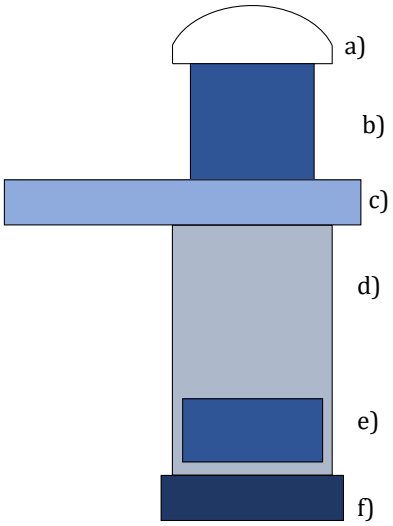

Figure 2.1: Schematic diagram of airglow camera system: a) all-sky lens, b) telecentric lens system, c) filter wheel, d) optical tube, e) re-imaging lens and f) CCD-detector.

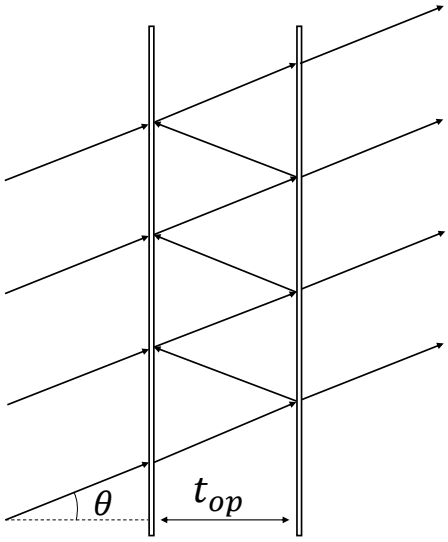

Figure 2.2: A schematic of an interferometer. Rays of light incident with an angle θ on two coated surfaces separated by an optical thickness t_{op}. Rays reflect and interfere several times as they pass through the interferometer.

surfaces with a cavity between them, seen in figure 2.2. The cavity can vary between the fraction of a millimeter to several centimeters. Rays of light incident to the filter reflect several times in the cavity, and interference occurs. As long as there is no phase difference between emerging wave-fronts, a transmission maximum forms. This happens when the optical path difference between rays is an integral number of whole wavelengths, i.e.: $m\lambda = 2t_{op}\, cos(\theta)$, $m = 1, 2, \ldots$. t_{op} is the optical thickness and θ is the angle of incidence. Narrowband interference filters are sensitive to changes in the incident angle θ. An increase in θ will cause a shift of the wavelength of peak transmission, in addition to increasing the bandwidth of the filter.

The telecentric lenses are vital in order to gain optimal filter results. The all-sky lens has a large angle of view, so rays from image-edges have large incident angles. Passing these rays through the filters would have resulted in poor filter performances. In a telecentric lens system the principal ray of all image-forming cones across the field of view cross the image plane parallel to the optical axis. The telecentric lens system focuses the all-sky image to an angle of incidence of only 7°, drastically decreasing both shifting of transmission peak wavelength and bandwidth broadening.

The optical tube and re-imaging lens are necessary in order to capture the 75 mm image

from the interference filter on to the CCD-detector, which is built for 25 mm cameras. The re-imaging lens simply images the filter on to the detector. The optical tube enables the re-imaging lens to be positioned at the correct distance without contaminating images with stray light. The CCD detector consists of a 25 mm square 1024x1024 pixel array array. The light imaged onto the detector causes each pixel to accumulate an electric charge proportional to the light intensity. It is mounted in an evacuated cell and cooled in order to reduce electronic noise.

The filter wheels are black disks with six large holes to hold narrowband interference filters. Five different filters have been used in different combinations at Halley and Rothera; an O_2 line filter, an OH broad band filter, a Na line filter, background (Bg) line filter and an auroral filter. Filter characteristics for the filters utilized at Halley during the Antarctic winter of 2000 are given in table 2.1. Images were obtained in the sequence: OH, Na, OH, Bg, OH, O2. With the exposure times given in table 2.1 and time to change filters, a full cycle takes about 5 min 45 s. The exposure time of OH images is smaller than the others since the OH airglow is more intense, and gives the series of OH images a high temporal resolution compared to other image series.

Table 2.1: The emission wavelength (λ_E), filter wavelength (λ_f), layer height and exposure time (t_{exp}) of the airglow emissions measured by the airglow imager at Halley Research Station in the Antarctic winter 2000. The type of emission is indicated in parentheses behind emission wavelength, while the full width at half maximum (FWHM) bandwidth of filters is indicated in parentheses behind filter wavelengths.

Species	λ_E (nm)	λ_f (nm)	Layer Height (km)	t_{exp} (s)
O_2	865.5 (bands)	865.5 (10)	94	90
OH†	400-4000 (bands)	715-950	87	15
Na	589.2 (line pair)	589.2 (2.5)	90	90
Bg	-	572.5 (2.5)	-	90

† with a notch at 865 nm to suppress the O_2 emission.

At KHO, all 6 filter disks are filled. Filter 1 is a blocked filter measuring dark current, while filter 4 measures background noise. Filters 2 and 3 measure auroral lines in the OH airglow spectra, while filters 5 and 6 measure isolated OH airglow lines. Filter characteristics are given in table 2.2. Images are obtained in the sequence 2, 3, 4, 5, 6, with a dark current image taken every 9th cycle. With the exposure times given in table 2.1 and time to change filters, a full non-dark current imaging cycle takes about 8 minutes and 49 seconds.

Table 2.2: Filter wavelength (λ_f) and exposure time (t_{exp}) of the filters utilized in the airglow imager at KHO during the winter 2021-2022. The FWHM bandwidth of filters is indicated in parentheses behind filter wavelengths. Filter 1 is a blocked filter measuring dark current, filter 4 is a background filter, while the other filters measure different lines in the OH-spectra.

Filter number	λ_f (nm)	t_{exp} (s)
1	BLOCKED	30
2	844.6 (1.85)	30
3	844.6 (1.8)	120
4	856.8 (1.83)	120
5	846.5 (1.8)	120
6	840.0 (1.8)	120

2.2 Image Filtering

There is a substantial intensity difference between auroral structures and airglow structures. Additionally, GWs have a relatively low contrast between peaks and troughs in airglow images. Hence, filtering is necessary in order to enhance auroral structures and GW structures. The filtering techniques primarily used in this thesis work are contrast-stretching and median-filtering. Contrast-stretching, or normalisation is a simple enhancement technique that attempts to improve the contrast of an image by stretching the range of intensity values to span a desired range of values. The operation is performed on each pixel, and defined as:

$$P_o = (P_i - l)\frac{\max - \min}{u - l} + \min, \tag{2.1}$$

where P_o and P_i denote the pixel output and pixel input respectively. [min, max] is the interval P_o lie within and $[l, u]$ is the interval of intensities in P_i to be normalized within [min, max]. In the thesis work, [min, max] = [0,65535] has solely been used. This corresponds to black and white in 16-bit grayscale images. This means all P_i below l are output as black, and all P_i above u are output as white. Figure 2.3 illustrates the relationship between P_i and P_o. Contrast-stretching is especially useful when trying to separate auroral and airglow structures, given their dissimilarity in intensity. The MATLAB function *imadjust* has been used to contrast-stretch images (MATLAB, 2020).

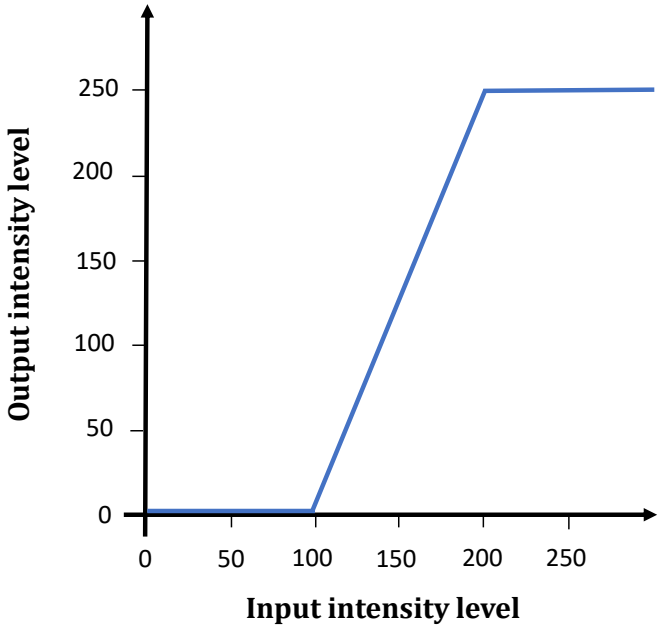

Figure 2.3: An illustration of contrast-stretching. For this particular case, all input pixels with intensity below 100 have an output intensity of 0, while all input pixels with intensity above 200 have an output intensity of 250. All input pixels with intensities within [100, 200] will be normalised to output intensities within [0, 250].

Median-filtering is a non-linear filtering technique that can be used to remove noise from an image. The principal idea of median-filtering is to replace each pixel of an image with the median of itself and its neighbouring points. One can imagine a window of size $[m, n]$ covering a part of the image. The middle pixel of the window is replaced with the median value of all the pixels in the window. See figure 2.4 for an illustration of an operation. Median-filtering has been performed using the MATLAB function *medfilt2* (MATLAB, 2020). It can be useful both in the removal of small-scale and large-scale noise. A median-filter alone will reduce the small-scale noise. Subtracting a large-scale median-filtered image from itself:

$$I = I - I_m, \tag{2.2}$$

where I is a 2D-array representing the image and I_m is the median-filtered of I, will reduce large-scale variations in an image. This technique has been widely used in the thesis work to remove background variations.

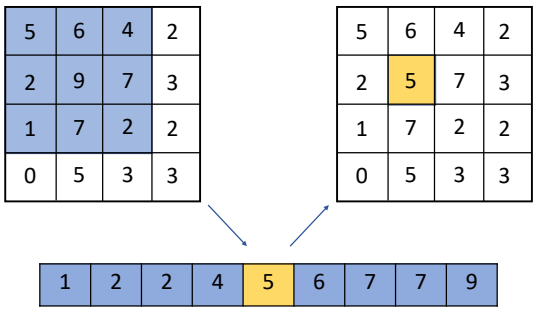

Figure 2.4: An illustration of median-filtering. A 4x4 matrix, representing an image is median-filtered using a 3x3 window shaded blue. The values of the window are ordered, and the median is found to be 5, shaded yellow. The middle value of the window is subsequently replaced by 5.

2.3 Geographical Projection

A problem associated with the utilization of all-sky lenses in airglow imaging is that linear wave patterns appear curved. The lens images in such a way that each pixel images equal angles of the sky (Garcia, 1997). In order to perform a measurement of geographical wave-parameters, and to more easily separate airglow and auroral structures, a geographical projection of the images is needed. Original image coordinates (i, j) do not have zenith in origin, are rotated slightly, so that north is not up. They are furthermore flipped with respect to east-west, so that west is towards right in raw airglow images. The first step of the projection performs a geometrical calibration which finds the zenith pixel of the images, and the image rotation with respect to geographical north. It also finds the number of pixels per radian in the image k_r. Images are then rotated, cropped and flipped (with respect to east and west), giving standard coordinates (f, g), where zenith is the origin, north is upwards and east is to the right. Subsequently, azimuth and zenith angles (az, z) of the standard coordinates are calculated using k_r. A geographical plane (x, y) tangential to the imager at airglow height is generated, and (az, z) is calculated for the geographical grid. Via the (az, z) coordinates, the standard coordinates (f, g) are transformed to geographical coordinates (x, y). See figure2.5a for an illustration of the coordinate mappings used in the projection. The image is afterwards interpolated onto the geographical plane using sinc-interpolation. Sinc-interpolation fits the continuous function:

$$I(x) = \sum_{n=-\infty}^{\infty} I[n] sinc\left(\frac{x - nX}{X}\right) \tag{2.3}$$

to the sequence of numbers I[n], where *sinc* denotes the normalized sinc function and X denotes the sampling period of $I[n]$.

Airglow layers are curved, meaning that representing them on a planar grid will introduce some error, but since the analysis area is orders of magnitude smaller than the area of the spherical shell at the height of the emission layer, this error is negligible (Garcia, 1997). See figures 2.5 for an example of how the projection routine works. Figure 2.5a shows the transformations between coordinate systems (i, j) and (x, y). Figures 2.5b, 2.5c and 2.5d show a raw OH airglow image, the raw image mapped to (f, g) coordinates with the (x, y) grid marked and the final, geographically projected image.

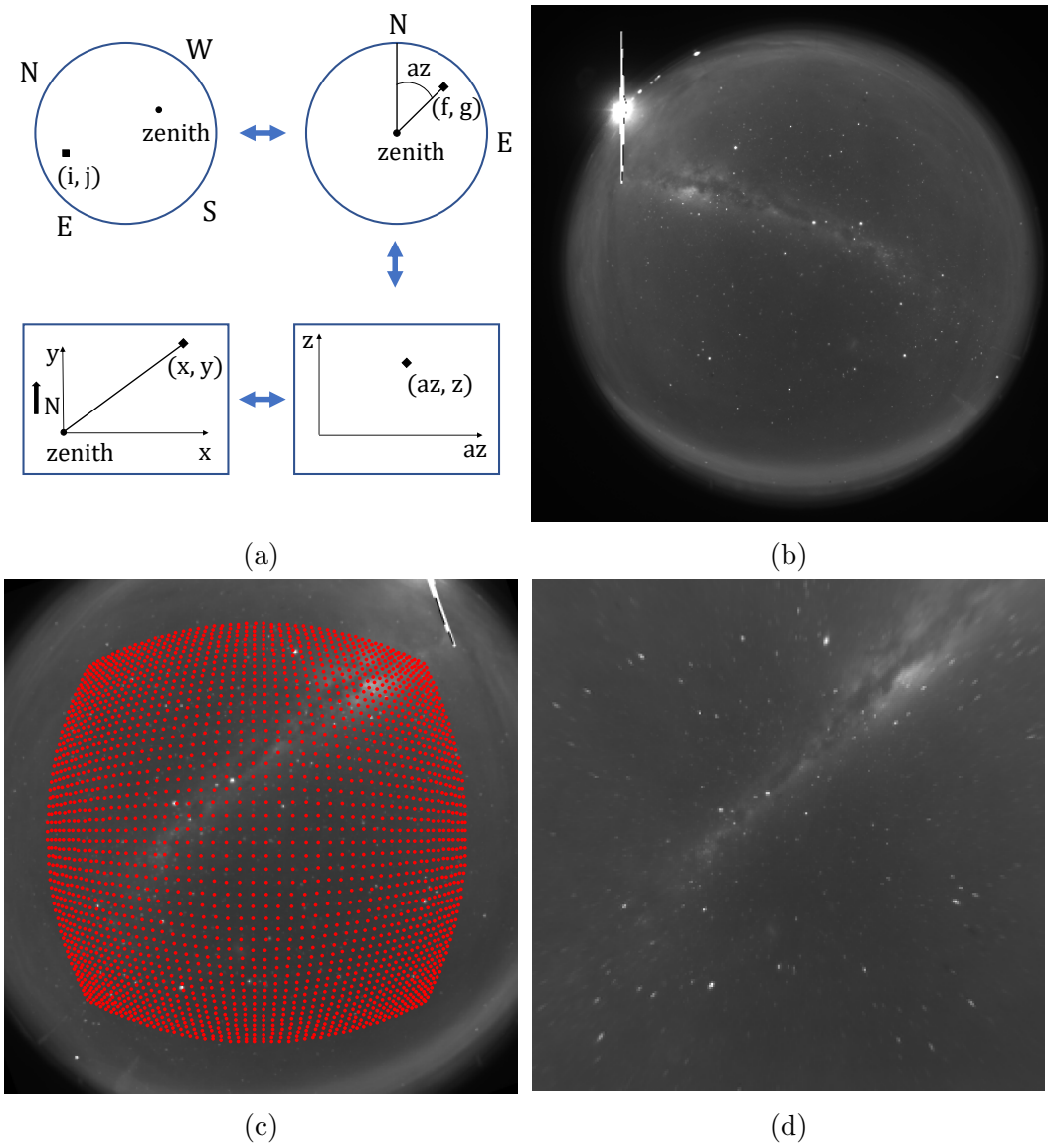

Figure 2.5: (a) The coordinate systems used in projection of airglow images. Adapted from Garcia et al., 1997. (b) A raw, i.e. in (i, j) coordinate system, airglow image. (c) The image in (b) mapped to (f, g) coordinates with every fifth entry of the geographical grid (x, y) marked with red dots. (d) The projected and interpolated image, i.e., (x, y) coordinates.

2.4 Wavelength Estimation

Estimating wavelengths and finger structure separations

Horizontal GW wavelengths λ_H and finger structure separations ΔX_{FS} are estimated using the geographically projected images. Wave and finger structure locations $\vec{r_{w,i}}$ and $\vec{r_{fs,i}}$ are found in each image of interest. Distances between consecutive $\vec{r_{w,i}}$ and $\vec{r_{fs,i}}$ are then calculated using the Pythagorean theorem:

$$\lambda_{H_i} = ||\vec{r_{pk,i+1}} - \vec{r_{pk,i}}||, \tag{2.4}$$

$$\Delta X_{FS_i} = ||\vec{r_{fs,i+1}} - \vec{r_{fs,i}}||. \tag{2.5}$$

Mean $\lambda_H = \overline{\lambda_{H_i}}$ and $\Delta X_{FS} = \overline{\Delta X_{FS_i}}$ and standard deviations σ for λ_{H_i} and ΔX_{FS_i} are calculated for each image. Means and standard deviations are also calculated for λ_H and ΔX_{FS} over entire events.

2.5 Wave Speed Estimation

In order to determine whether the atmospheric waves are mesospheric bores or not, wave propagation speeds c have been estimated. Neither images from KHO nor Na images have a sufficient temporal resolution to estimate wave speeds, so OH images from BAS have been used. Images are first filtered using the techniques presented in section 2.2. First, large-scale noise is removed using the technique described by equation 2.2 with coefficients $[m_l, n_l] = [15, 15]$. Then small-scale noise is removed using a median-filter with coefficients $[m_s, n_s] = [5, 5]$. Subsequently, the images are contrast-stretched with coefficients $[l, u] = [0, 5]$. Waves will after this filtering appear as completely white and completely black stripes, see figure 2.6 for an example of how an image looks after this kind of processing.

After filtering the images, intensity profiles c_i along a line segment parallel to the direction of wave propagation are obtained for each image I_i. Then, the intensity profiles are interpolated along a 1000 entry long linearly spaced vector $x = [0, ..., N]$, where N is the length of the intensity profiles c_i. This increases the resolution of the intensity profiles, improving estimation results. Subsequently, the estimated cross-correlations between the intensity profile from the first image and the other images are calculated:

$$\hat{R}_{j1}(m) = \begin{cases} \sum_{n=0}^{N-m-1} c_j(n+m)c_1^*(n), & m \leq 0 \\ \hat{R}_{1j}^*(-m), & m < 0, \end{cases} \tag{2.6}$$

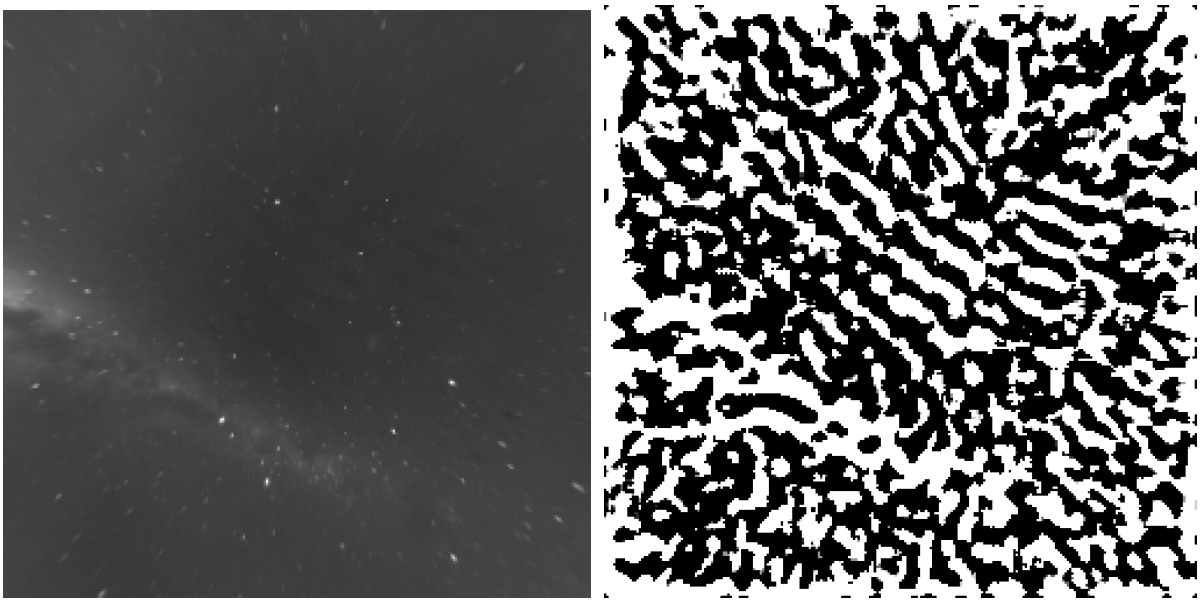

(a) (b)

Figure 2.6: Highlighting GW structures for intensity profile acquirement. (a) Projected OH airglow image with barely visible GW structures in the zenith. (b) Filtered version of (a) highlighting the zenith GW structures.

where N is the length of the intensity profiles and $j \neq 1$. $\hat{R}_{j1}(m)$ is a measure of the similarity between lagged copies of the intensity profile c_1 and the other intensity profiles c_j as a function of lag. $\hat{R}_{j1}(m)$ is calculated using the MATLAB function *xcorr*, which returns the cross-correlation vector (MATLAB, 2020):

$$r_{m,j} = \hat{R}_{j1}(m - N), m = 1, 2, ..., 1999. \tag{2.7}$$

Additionally, it returns the corresponding lag indices $l_m = -N, ..., 0, ..., N$. For each j, $r_{m,j}$ takes its maximum value at the lag index $l_{max,j}$ where the lagged c_1 is most similar to c_j. The maximum correlation lag indices $l_{max,j}$ thus indicate how much the wave has moved for each image. Lag indices corresponding to a wave movement opposite to observed are discarded. To estimate the wave speed, a linear regression model has been fitted between the maximum correlation lag indices and difference in imaging time between I_1 and I_j, Δt_j. Note that $l_{max,j}$ unit is pixels. In order to obtain wave speeds in m/s, $l_{max,j}$ are multiplied with the number of meters per pixel in a projected BAS airglow image, which is $k = 1176.5$ m/pixel. The estimated wave speed is given as the slope of the linear regression model with the standard error of the slope: $c \pm \sigma_c$.

CHAPTER 3

Results

A substantial portion of the thesis work has focused on finding events where finger-structures and GWs can be seen simultaneously, and additionally seem to relate. Three events were found from the Halley Research data, and these are listed by the time of first GW observation, finger structure observation and last GW observation in table 3.1. No events were found in Rothera data. One event was found in Svalbard data, but this event was not analysed further due to a low wavelength compared to spatial resolution. See figure A.1 in appendix for airglow images of this event. This section presents both qualitative and quantitative data from the three events imaged at Halley. OH images were contrast-stretched in order to enhance auroral structures. Na images were similarly contrast-stretched in order to enhance airglow structures. Aurora-enhanced images and airglow-enhanced images are presented for each event, providing a qualitative overview of how finger structures and GWs relate. A comparison of finger structure separation and wavelengths estimated from images where finger structures and GWs were visible are subsequently presented in order to provide a more quantitative analysis. Additionally, an estimated wave propagation speed for each event is presented. All times are given in Universal Time (UT).

3.1 Structures

Figures 3.1, 3.2 and 3.3 show contrast stretched, geographically projected airglow images taken with Na and OH filters. In the images, geographic north is up and east is right. All images are taken at Halley Station, and are from June 3rd, 4th and 7th 2000 respectively.

The images are chosen to show the 30-70 minute lasting events in as few pictures as possible. Images a)-c) in each figure are from the Na-filter, while images d)-f) are from the OH-filter. Each row shows images taken at approximately the same time side-by-side, showing important moments from each event. The top row, images a) and d) of each figure, shows the first spotting of the GWs believed to be connected to the finger structures. The middle row, images b) and e) of each figure, shows the finger structures, with the structures circled. The bottom row, images c) and f) of each figure, shows the last spotting of the GWs for each event in figure 3.1 and 3.2. In figure 3.3, the bottom row depicts another finger structure. Moonlight contaminated the images and made it difficult to detect both auroral structures and GW structures, so no end time was found to the June 7th 2000 event. Time of capture t for each image is obtained from the header of the image file. Note that the image header times t for some OH and Na images are inconsistent with the exposure times and sequence of imaging as described in section 2.1. The reason for this is unknown.

Table 3.1: Time of first observation of GWs, finger structures, as well as last observation of GWs for each event analysed in this thesis in UT. Note that the first observation of GWs mean first observation of GWs that connect to the finger structures.

Date	First GW	Finger structures	Last GW
June 3rd 2000	02:35	02:46	03:06
June 4th 2000	04:27	05:08	05:35
June 7th 2000	07:43	08:08	-

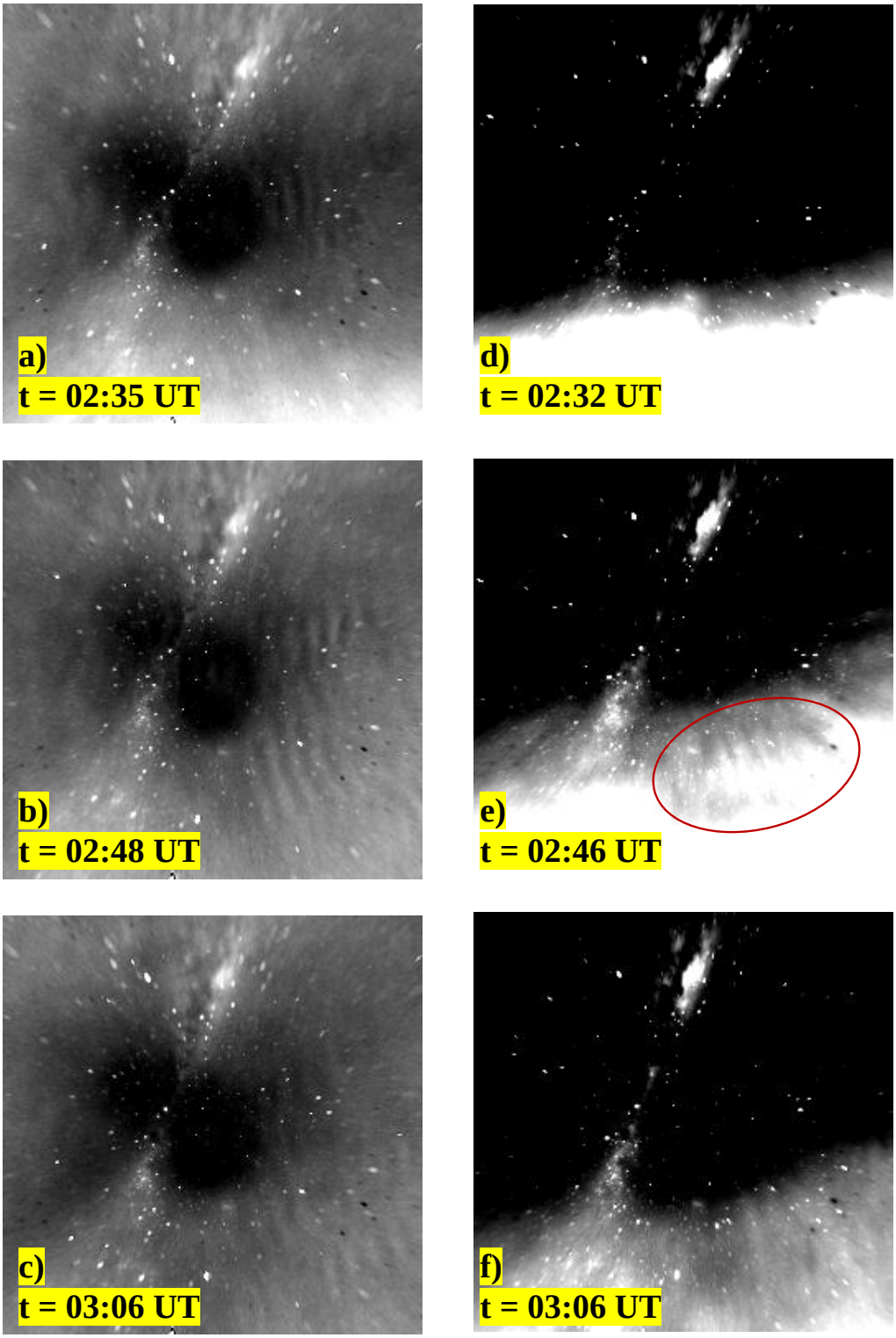

Figure 3.1: Contrast stretched airglow images taken at times t, June 3rd 2000. a)-c) are images taken with Na-filter and have contrast stretching parameters $[l, u] = [3900, 5100]$. d)-f) are taken images taken with OH-filter and have contrast stretching parameters $[l, u] = [24700, 32950]$. The finger structures are circled in e).

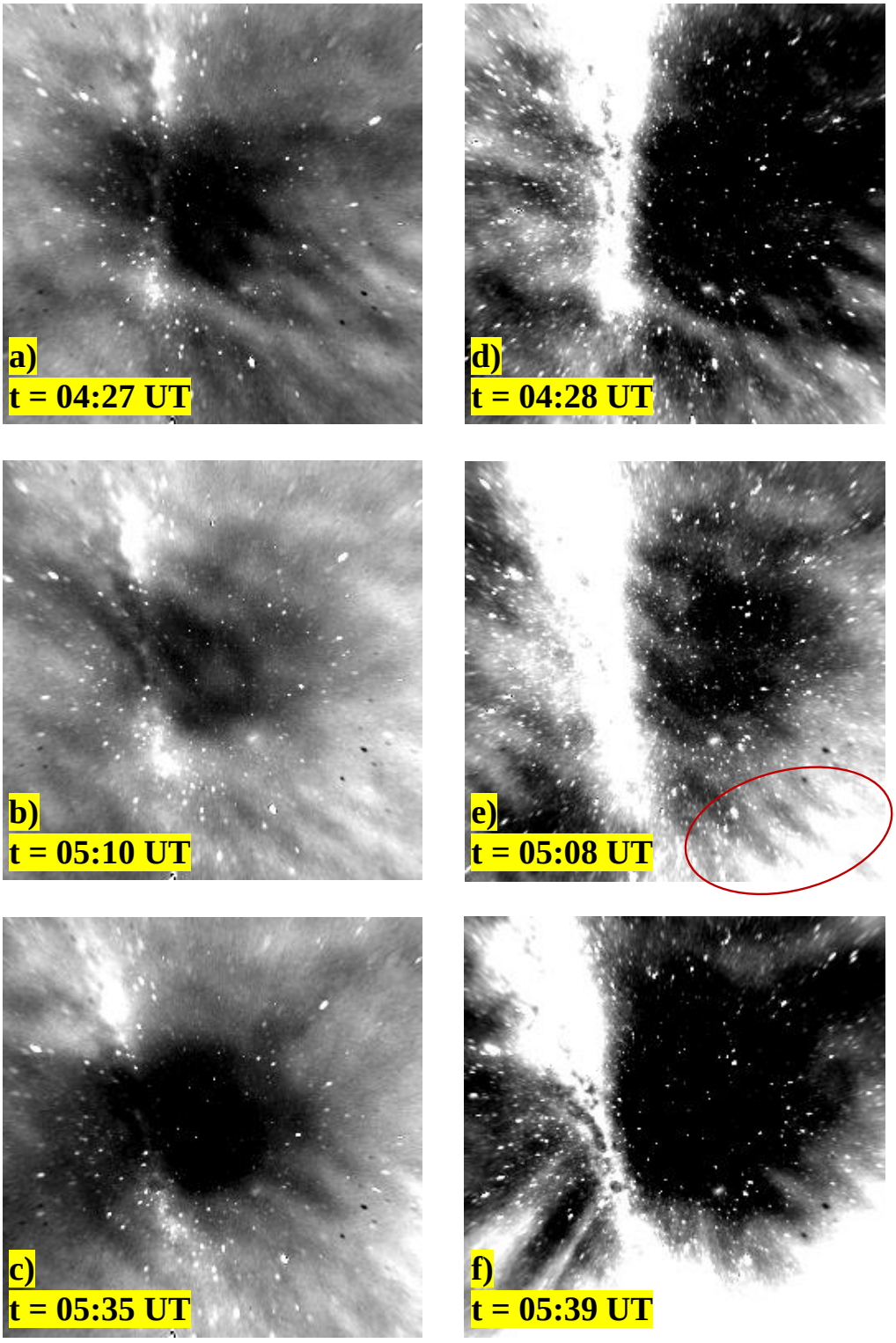

Figure 3.2: Contrast stretched airglow images taken at times t, June 3rd 2000. a)-c) are images taken with Na-filter and have contrast stretching parameters $[l, u] = [3545, 5350]$. d)-f) are taken images taken with OH-filter and have contrast stretching parameters $[l, u] = [14150, 18653]$. The finger structures are circled in e).

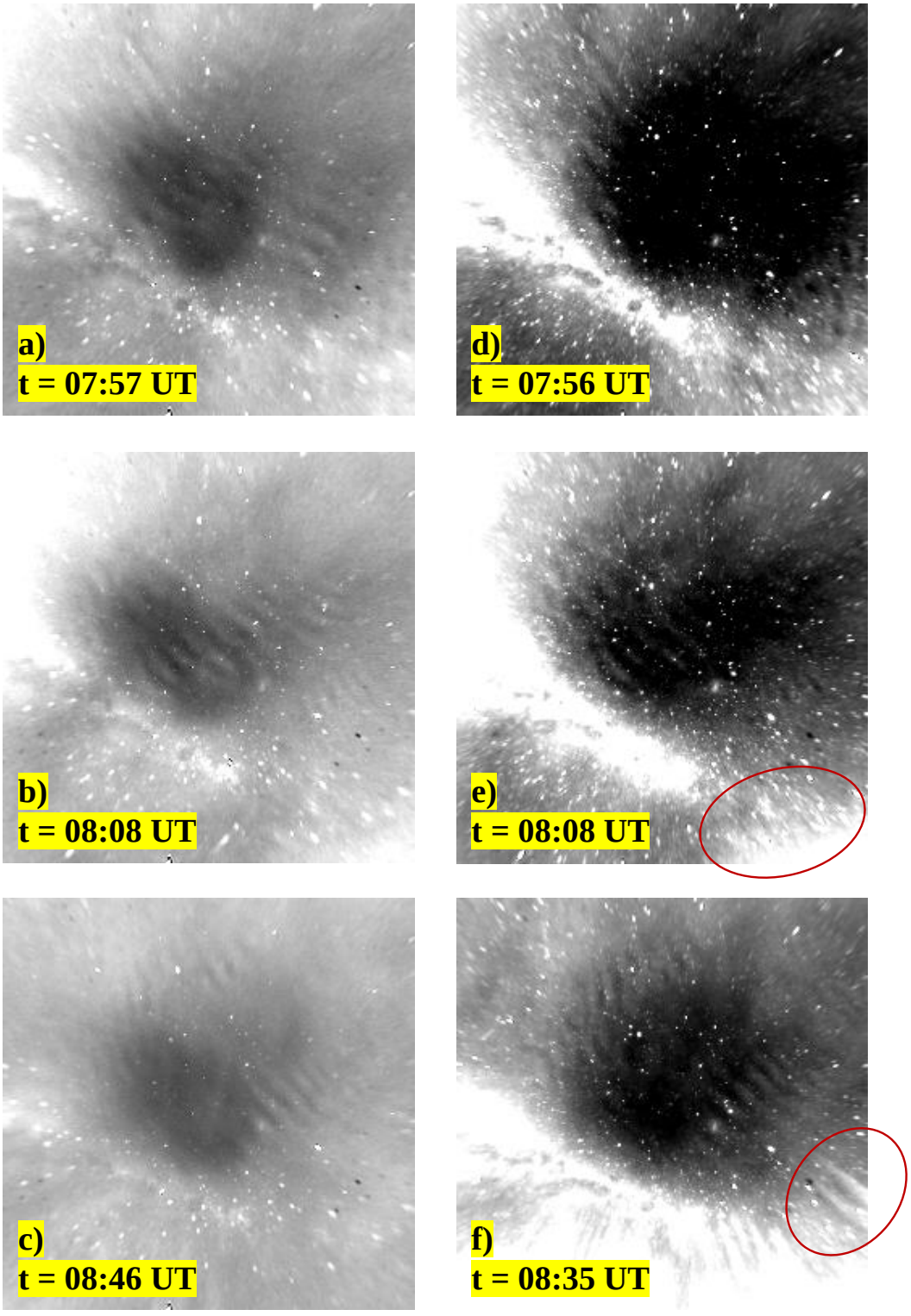

Figure 3.3: Contrast stretched airglow images taken at times t, June 3rd 2000. a)-c) are images taken with Na-filter, while d)-f) are taken images taken with OH-filter. The finger structures are circled in e) and f). Contrast stretching parameters: $[l, u]$ =[2490, 5000] for a) and b), $[l, u]$ =[2500, 6620] for c), $[l, u]$ =[12515, 17175] for d) and e) and $[l, u]$ =[15160, 22620] for f).

3.2 Wavelengths

Estimated wavelengths and finger structure separations

Estimated mean horizontal GW wavelengths (λ_H) and finger structure separations (ΔX_{FS}) $\pm$ standard deviation for the three events are given in table 3.2. Figures 3.4 show the temporal evolution of λ_H (yellow) and ΔX_{FS} (green) for June 3rd, 4th and 7th 2000 respectively. The error bars correspond to the standard deviations of the measurements taken at each time. λ_H and ΔX_{FS} have been estimated as described in section 2.4, and are multiplied with the number of meters per pixel in the projected airglow images (k =1176.5 m/pixel) to obtain wavelengths and separations in km.

Table 3.2: Estimated horizontal GW wavelength (λ_H) and finger structure separation (ΔX_{FS}) for the events analysed in the thesis work. Given as mean $\pm$ standard deviation for the three finger structure events analyzed in this thesis work.

Date	λ_H (km)	ΔX_{FS} (km)
June 3rd 2000	16.45 $\pm$ 1.00	15.15 $\pm$ 0.71
June 4th 2000	24.42 $\pm$ 3.65	25.24 $\pm$ 2.25
June 7th 2000	16.08 $\pm$ 1.63	13.75 $\pm$ 1.52

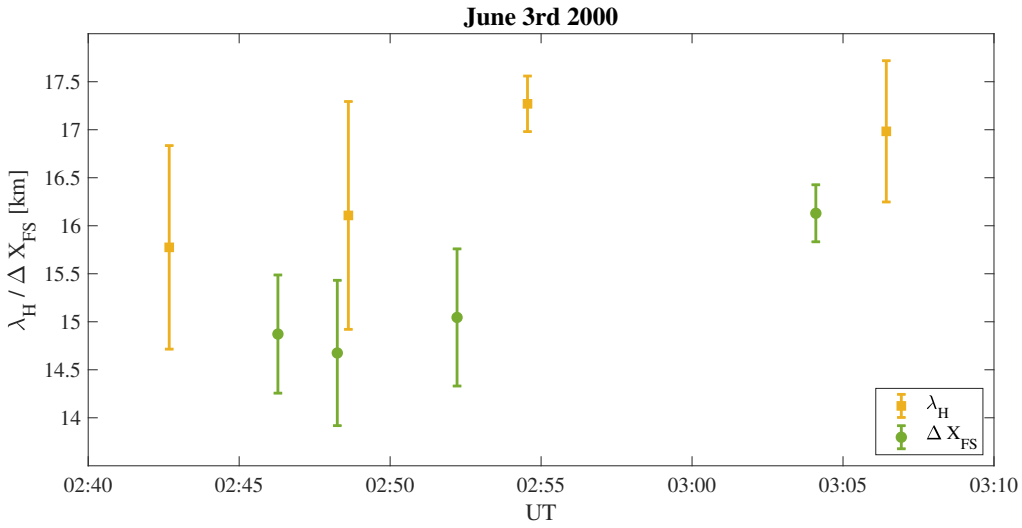

(a)

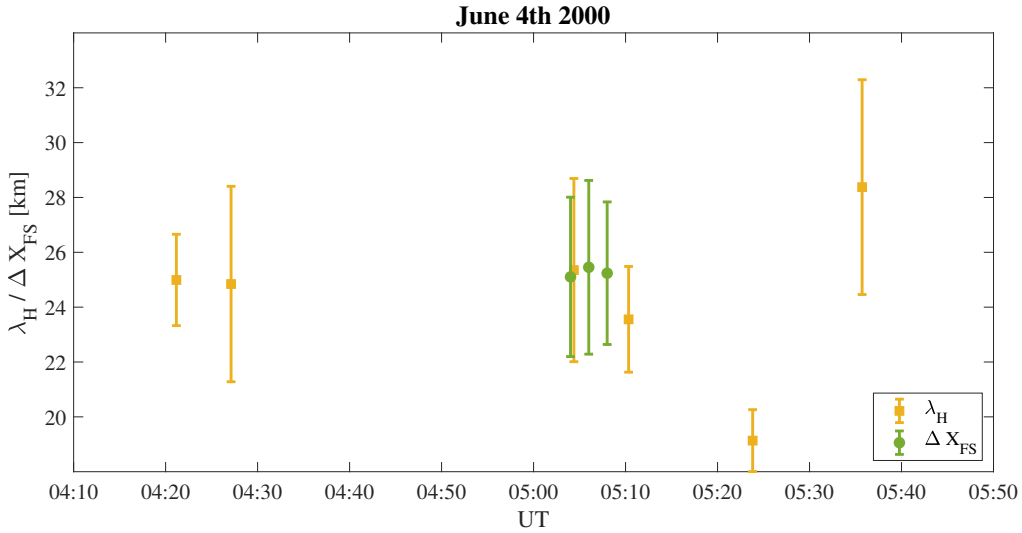

(b)

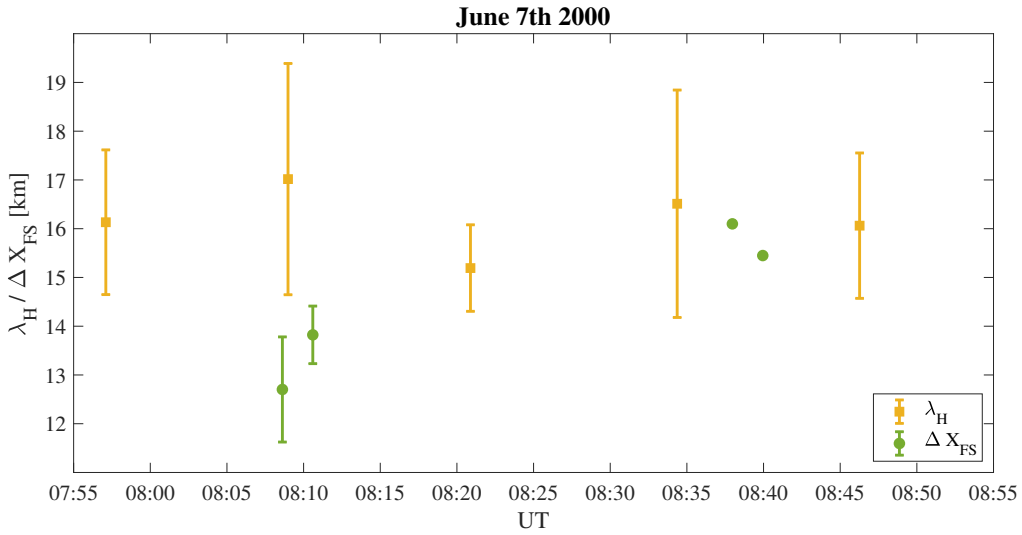

(c)

Figure 3.4: Temporal evolution of horizontal GW wavelength (λ_H) and finger structure separation (ΔX_{FS}) for Jun 3rd 2000, Jun 4th 2000 and Jun 7th 2000 (error bars from standard deviation).

3.3 Wave Propagation Speed

Estimated wave propagation speeds c and standard errors σ_c are given in table 3.3, as well as the time of capture and the number of images used for estimation. They have been estimated using the method described in section 2.5, and the images are taken with the OH filter. Figure 3.5 shows the maximum correlation lag indices $l_{max,j}$ as a function of difference in imaging time Δt_j between first image I_1 and consecutive images I_j for each event. A linear regression model is fitted to the data, whose slope gives the estimated c. Figures 3.6, 3.7 and 3.8 show normalised intensity profiles c_i from processed, consecutive images I_i for each event. The intensity profiles are from the same image slice, and parallel lines are drawn across each figure. The slope of the parallel lines correspond to the estimated propagation speed c. The lines are drawn between a point x_1 corresponding to a wave peak of the intensity profile c_1 in subplot $i = 1$ and points $x_j = x_1 + \Delta x(i-1)$ in each subplot i =2, 3, 4, 5. $\Delta x = c\Delta T$, where ΔT is the cadence time of the images, meaning that Δx is the movement of a wave at speed c in the time between imaging of I_i and I_{i+1}. The fit between parallel lines and wave peaks of intensity profiles c_i thus provides an indicator of the accuracy of the estimated speed.

Table 3.3: Estimated wave propagation speeds c, time of capture and number of images used in estimation for the three events analysed in the thesis work. Estimated speeds are given as regression slope ± standard error of regression slope.

Date	c (m/s)	Time of capture (UT)	Number of images
June 3rd 2000	16.16 ± 0.69	02:42-02:54	7
June 4th 2000	22.63 ± 3.02	05:04-05:11	5
June 7th 2000	9.02 ± 0.31	08:22-08:34	6

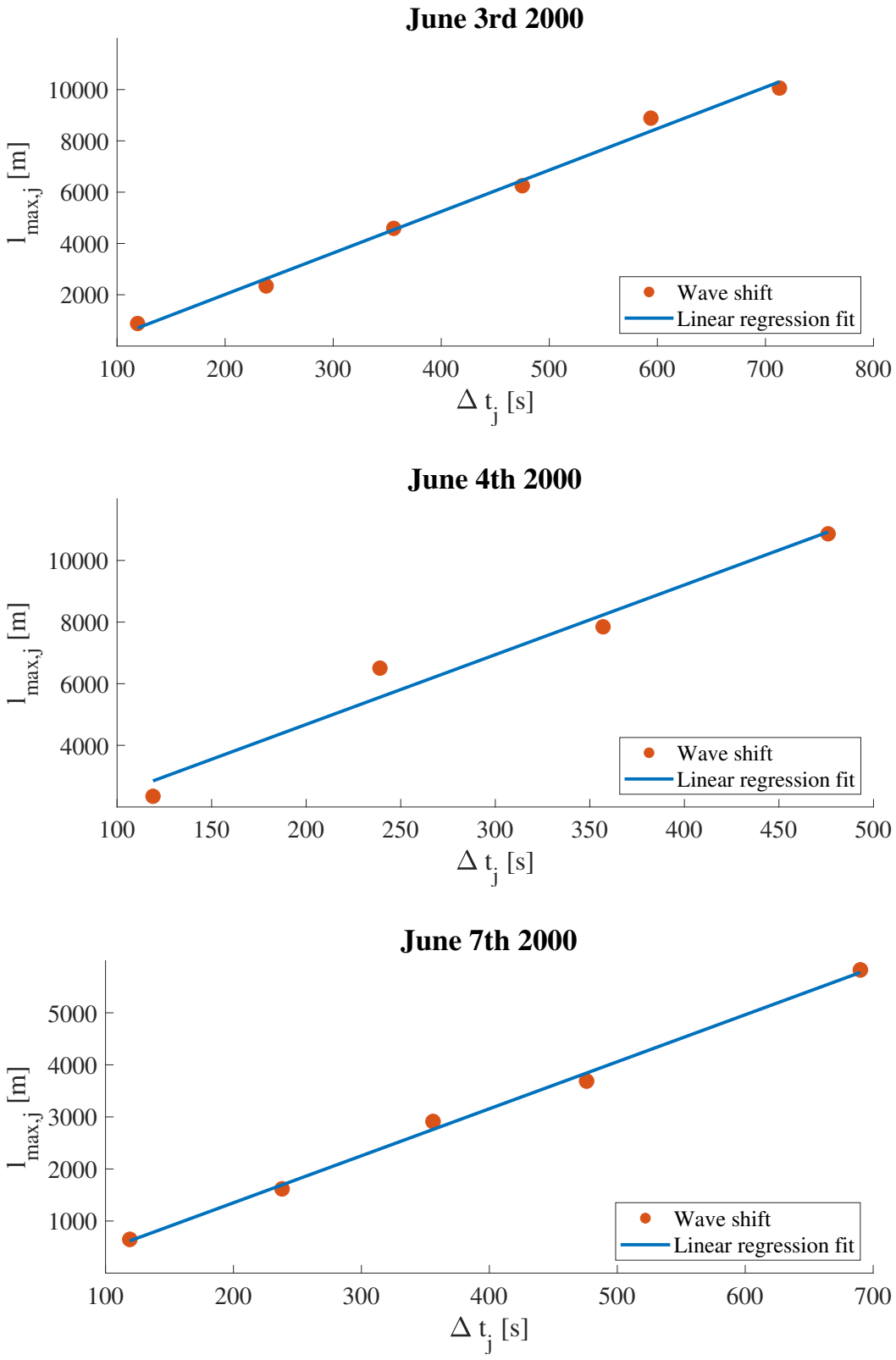

Figure 3.5: Maximum correlation lag indices $l_{max,j}$ (red circles) from intensity profiles as a function of difference in time of capture Δt_j between the first image of a series I_1 and the following images I_j. Calculated for a series of consecutive OH airglow images from June 3rd, 4th and 7th 2000. A linear regression model (blue lines) is fitted to data from each event. The slope of the linear regression model gives the estimated speed.

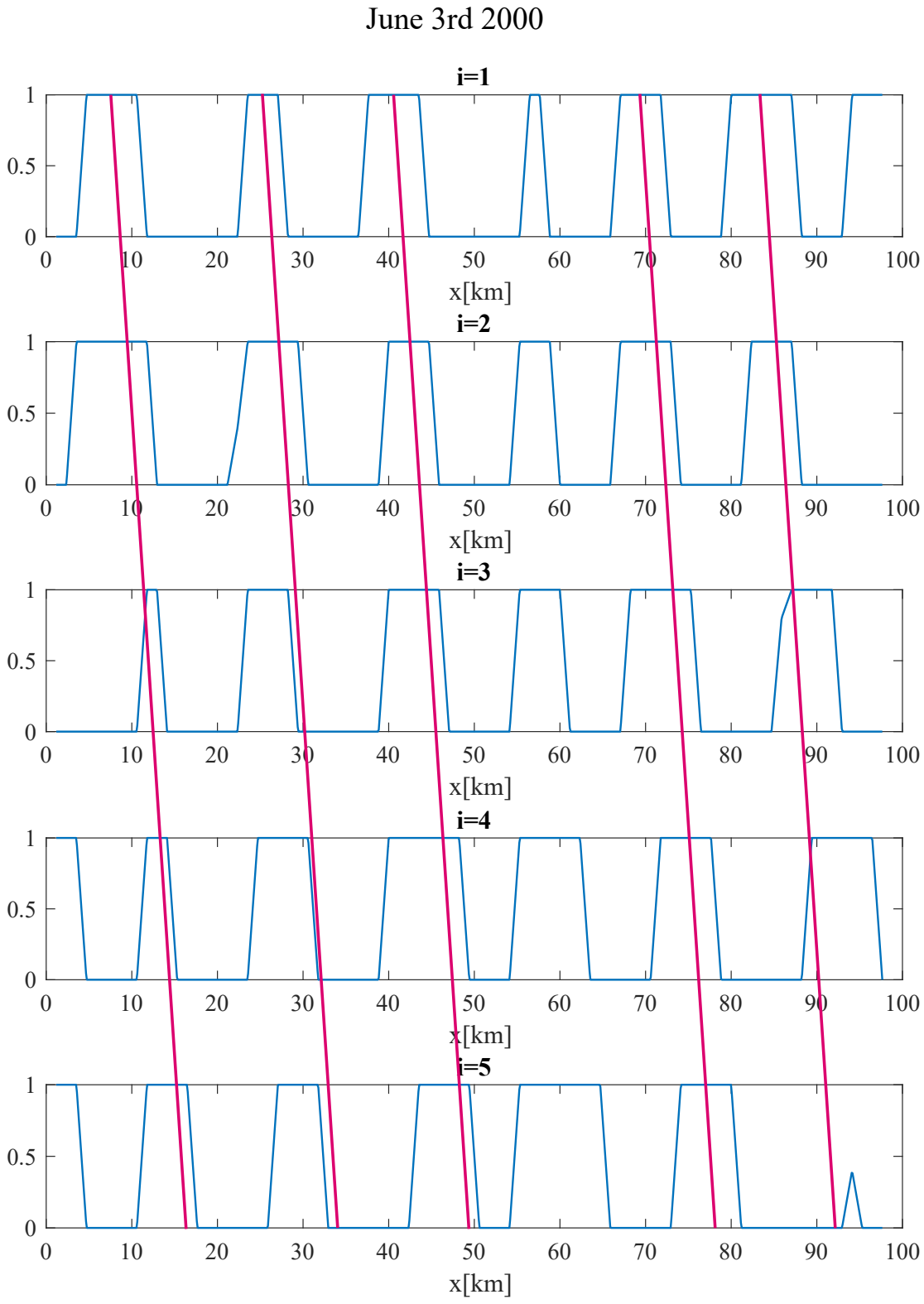

Figure 3.6: Intensity profiles c_i (blue lines) from airglow images taken June 3rd 2000. Parallel pink lines whose slope is given by the estimated speed c are drawn across.

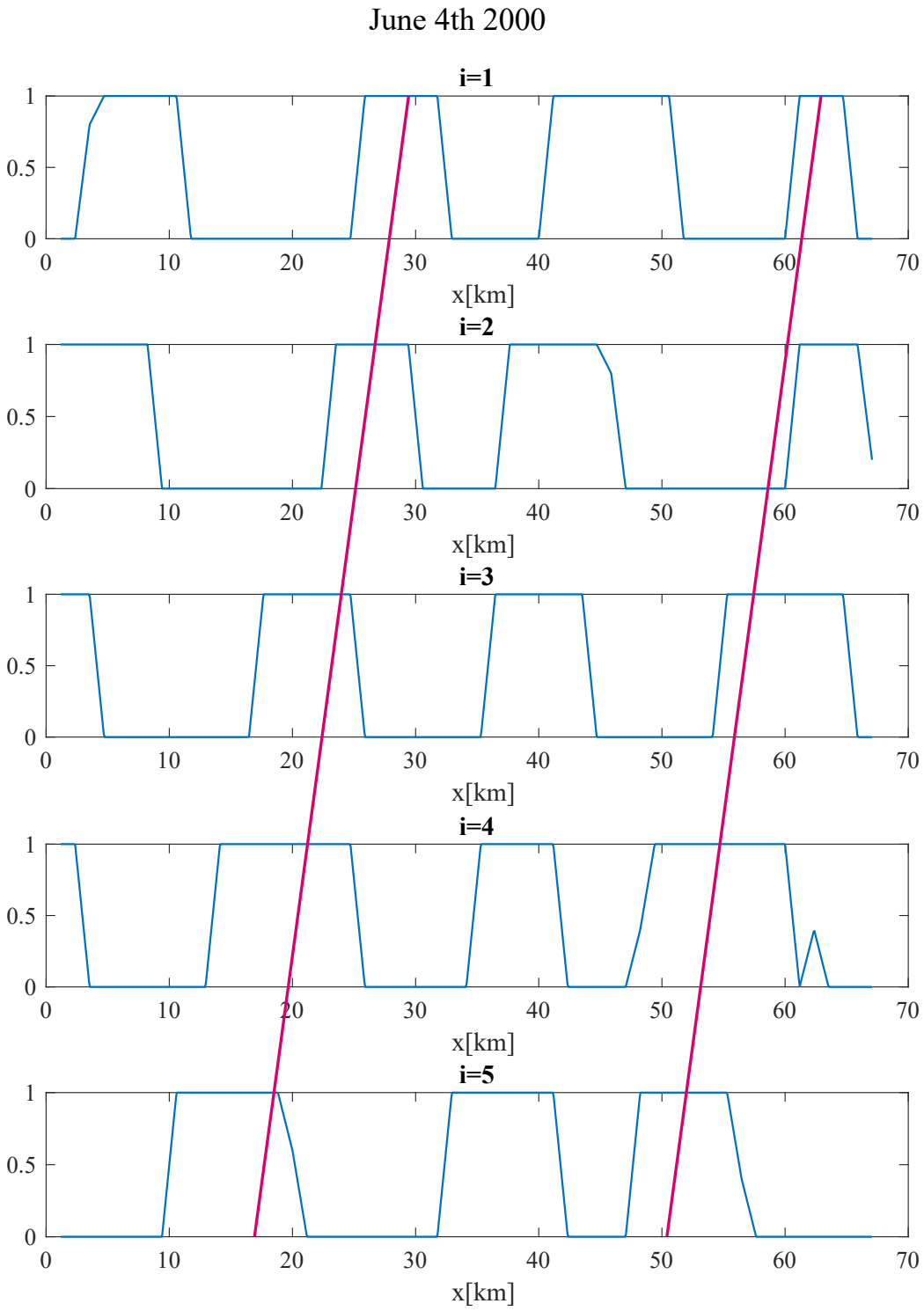

Figure 3.7: Intensity profiles c_i (blue lines) from airglow images taken June 4th 2000. Parallel pink lines whose slope is given by the estimated speed c are drawn across.

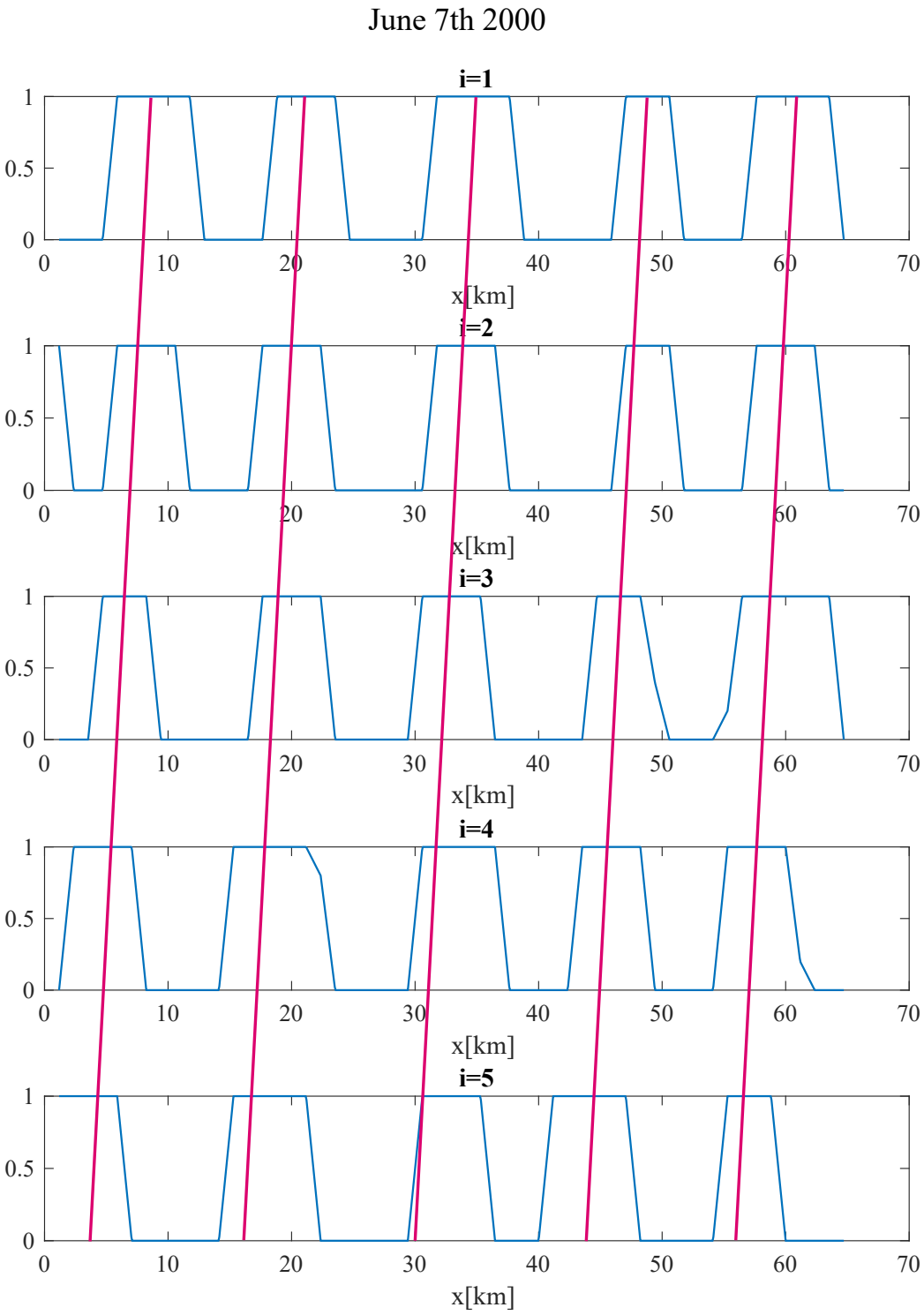

Figure 3.8: Intensity profiles c_i (blue lines) from airglow images taken June 7th 2000. Parallel pink lines whose slope is given by the estimated speed c are drawn across.

CHAPTER 4

Discussion

4.1 Instruments and Image Processing

There are several issues associated with airglow imaging, especially airglow imaging whilst aurora. First of all, the images are vulnerable to light contamination, such as aurora, stars, moonlight and sunlight. Especially the Milky Way is a major source of light contamination in the southern hemisphere, and is difficult to remove from images even with filtering. Additionally, the images are affected by both the Van Rhijn effect and vignetting. The Van Rhijn effect is caused by an increase in the contribution of an emission layer for off-zenith angles, and increases the intensity towards image edges. This is not a significant issue for the cropped and projected images, as the image edges are cut out. Some contribution is nevertheless present even in the cropped images. Vignetting is an effect naturally occurring in all lenses, and reduces the observed intensity near edges of field of view. A striking feature in the projected airglow images is the drop of intensity close to the zenith, which is especially noticeable in the sodium airglow images (images a) to c)) in figures 3.1, 3.2 and 3.3. The drop is probably a combination of the Milky Way's contribution (which rotates around the zenith) and the Van Rhijn effect. The drop of intensity in the zenith of projected images may also be amplified by the interpolation. The projection grid, as seen in figure 2.5c has fewer grid points towards the zenith, resulting in more interpolated pixels off-zenith in the projected and interpolated image. The interpolated images may thus be more affected by stars and the Van Rhijn effect off-zenith, enhancing the contrast difference between zenith and off-zenith areas of the images. The contributions from light contamination and optical effects are possible to reduce with more sophisticated

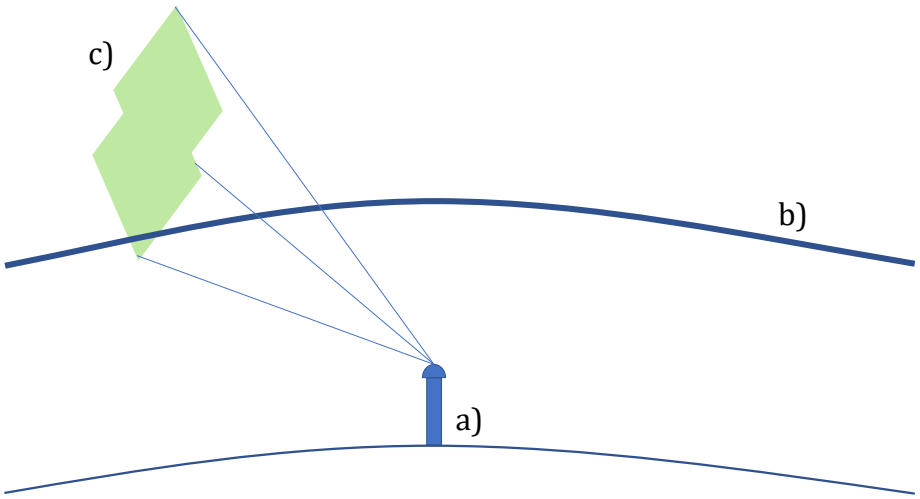

Figure 4.1: Illustration of all-sky imaging of aurora and airglow simultaneously. a) An all-sky airglow imager, b) airglow layer and c) vertical auroral structure. The vertical auroral structure is mapped as a horizontal structure.

filtering techniques, involving flat-fielding and a star-removal algorithm. The results from this more sophisticated routine were deemed unsatisfactory, with wave structures being filtered out, and the Milky Way dominating. These techniques have thus not been used, but a better implementation of them could give better results.

The airglow layers imaged extend an altitudinal range of 20-40 km. Auroral structures on the contrary may extend altitudinal ranges of several hundred km. Two-dimensional airglow imaging of aurora may therefore cause vertical auroral structures spanning large altitudinal distances to be mapped horizontally, as shown in figure 4.1. It is necessary to be aware of this effect while analysing airglow images, as it complicates analysis of auroral structures. Tall auroral rays mapped horizontally can resemble finger structures, but two points indicate that the finger structures presented in figures 3.1, 3.2 and 3.3 not are tall rays. First of all, finger structures with approximately same wavelength are present in several images, as shown in figures 3.4. Auroral structures would most likely not show this temporal reliability. Secondly, Na airglow images are filtered at a wavelength and bandwidth that strongly reduces auroral activity in the images. They will thus primarily depict horizontal sodium structures, although the filter is susceptible to bandwidth increase and shift in wavelength of peak transmission towards image edges. Several sodium airglow structures highly resemble the finger structures and can be traced to them, a second indication of the finger structures not being tall rays, but airglow structures illuminated by the aurora.

4.2 Bores, Boring or Auroral?

In the airglow images from June 3rd 2000, seen in figure 3.1, GW structures stretching north-south are first visible at 02:35 UT. This is 11 minutes before the finger structures, which have approximately the same direction, appear at 02:46 UT. The last sighting of the GWs is at 03:06 UT, with structures still displaying an orientation approximately north-south. This strongly indicates that the same GWs is seen at 02:35 UT and 03:06 UT, and additionally that the finger structures are wave ridges of these GWs illuminated by aurora. The aurora is already present at 02:32 UT, and it can therefore not be concluded that the wave generation is independent of the aurora. It should however be mentioned that GWs with a different orientation are visible prior to the aurora, which cannot directly relate to the finger structures. It should furthermore be noticed that the aurora is barely visible at 03:06 UT, when the GWs were last spotted. This suggests that the wave structures are not an auroral phenomena. The measured horizontal wavelength λ_H and finger structure separation ΔX_{FS} are comparable. Figure 3.4a furthermore shows that ΔX_{FS} increases when λ_H increases. It should also be noted that λ_H changes little during the event, indicating a low auroral impact on the Na airglow structure.

In the airglow images from June 4th 2000, seen in figure 3.2, GW structures stretching northwest-southeast are visible in the Na image from 04:27 UT. The OH image from 04:28 UT shows that there is a low auroral activity at this time, with some GWs also visible off-zenith. At 05:08 UT three clear finger structures are seen in the OH image, and the 05:10 UT image shows GWs at approximately the same place. Both the GWs and the finger structures have a similar orientation as the GWs seen in the image from 04:27 UT. At 05:35 UT, the last observation of the northwest-southeast oriented GWs is made. It is still high auroral activity at 05:39 UT. In this event, GWs with similar orientation and wavelength are present for more than one hour, and the finger structures seem to have the same orientation and separation as the GWs, again suggesting that the finger structures are GWs illuminated by the aurora. Furthermore, no aurora is present as the wave is first observed, indicating that wave generation is independent of aurora for this event. Aurora is however still seen after the GWs no longer are observable. The measured horizontal wavelength λ_H and the finger structure separation ΔX_{FS} are also comparable in this event, notice especially how similar the quantities are between 05:00 UT and 05:10 UT in figure 3.4b. Additionally, λ_H is fairly constant throughout the June 4th event as well, even though the event lasts for 68 minutes.

In the airglow images from June 7th 2000, seen in figure 3.3, at least two GW structures are visible at 07:57 UT in the Na image, but the ones most likely connecting to the finger

structures are the zenith structures approximately stretching northwest-southeast. The OH image from 07:56 UT shows low auroral activity. At 08:08 UT, the Na image once more shows what seems to be several structures, at a slightly different angle than at 07:43 UT. The OH image from 08:08 UT shows what resembles finger structures in the aurora, oriented northwest-southeast. The OH image from 08:35 UT also shows what seems to be finger structures, and following these structures into the zenith they seem to connect to some faint GW structures. Given that there are only two fingers, caution should be shown classifying these as finger structures. Preferably, more than two fingers should be visible for it to be categorized as a repeating finger structure pattern. Nevertheless, the fingers were visible in consecutive images, indicating that the structures not were tall auroral rays. The Na image from 08:46 UT shows that GW structures are still present with a northwest-southeast orientation, one hour past the first spotting of a GW with similar orientation. After 08:46 UT, the moonrise made accurate analysis difficult, so it has not been possible to determine an end time for the GW event or the auroral activity. This event showed the largest deviation between λ_H and ΔX_{FS}, although they still are similar. It should be noted from figure 3.4c that ΔX_{FS} deviates significantly from λ_H by around 4.5 km in images taken around 08:08 UT, but is far more similar around 08:35 UT. This might mean that the structures seen at 08:08 UT not are finger structures. It should also be noticed that λ_H is reasonably constant throughout the 49 minute event, and has a standard deviation of only 1.63 km.

The estimated wave propagation speeds c from each event, as shown in table 3.2, seem to be fairly accurate. Figure 3.5 shows that the linear regression fits the data well for all three events. The parallel lines in figures 3.6, 3.6 and 3.8 furthermore fit reasonably well with the wave peaks of the intensity profiles c_i, indicating that the method is satisfactory. The relative standard error of the estimated speed of June 4th is relatively high at 13.3 %, compared to the estimated speeds of June 3rd and 7th, which have relative standard errors of 4.3 % and 3.4 %. This might be due to the high wavelength compared to the length of the intensity profile. There also seems to be some noise in the intensity profiles, as seen in intensity profile c_3 in figure 3.7. The estimated velocities are a clear indication of all three waves being normal GWs, and not mesospheric bores, which have showed speeds above 60 m/s. Furthermore, no bore-typical bright or dark front is seen in front of the waves. Analysis in the O_2 or O airglow layers could have been performed, to see if the waves showed symmetrical features, but this has been deemed unnecessary given the low estimated speeds. A noticeable aspect of the estimated wave speeds is that they have very low phase speeds, well outside of the typical range in the climatology study of Nielsen et al. (2001). This might indicate that the wave speed estimation is flawed. One

apparent weakness in the estimation can be seen in figure 2.6; the filtering technique can create wave-like structures that at least not undeniably are wave structures. Choosing line segments that only obtain the intensity profiles of waves nevertheless seems to have been successful, as per visual inspection. Another possible flaw is that the incorrect direction of propagation has been observed, although visual inspection deems this unlikely. There is also a possibility that the wave has moved one or several wavelengths more than estimated by the cross-correlation calculation, giving a lower estimated speed. Assuming that waves have moved one wavelength λ_H, during cadence time Δt ≈119 s, more than estimated, this can be corrected by adding a term $\Delta c = \lambda_H/\Delta t$ to each estimated speed. Corrected speeds will then be around 154 m/s, 227.8 m/s and 143 m/s for June 3rd, 4th and 7th 2000 respectively, which has to be deemed highly implausible, considering results from the climatological study from Halley.

Wavelength and finger separation estimation could have been performed with more sophisticated methods, as the method pointing out finger structures and wave peaks have a large uncertainty of measurement. One possible technique is a standard two-dimensional Fourier analysis, as described by Garcia et al. (1997). This analysis requires the more sophisticated filtering techniques previously described, which filtered out interesting wave structures. Another possibility would have been to do a filtering similar to the one used in wave propagation speed estimation, as described in section 2.5, and then obtain intensity profiles along a constant image slice. This technique was satisfactory for certain images, such as for the images used to estimate wave propagation speed, but the long temporal scale of the events made this difficult. Waves were sometimes visible in zenith, and sometimes visible off-zenith, so that measuring intensity profiles across a constant image slice was unfeasible. Nevertheless, the measurements seem reasonable considering the low standard deviation and temporal development.

The dune events studied by Palmroth et al. (2020) and Grandin et al. (2021) were by triangulation determined to reside at around 100 km altitude, close to the altitude of the airglow layers analysed in this thesis work, which are in the range of 87-90 km. It is thus logical to compare wave parameters, especially considering that GW parameters are altitude-dependent. The dune events had estimated wavelengths in the range of 40-45 km, significantly larger than the λ_H and ΔX_{FS} estimated in this thesis work, which were in the range of 13-25 km. It is however worth noting that both dune wavelengths, λ_H and ΔX_{FS} are comparable to typical wavelengths from the climatological study of mesospheric GWs over Halley, found to be within the range of 15-40 km (Nielsen, 2001), as well as previously observed mesospheric bores, which had wavelengths in the range of 18-30 km (Taylor et al., 1995; Nielsen et al., 2006). Both the dune events and the events

analysed in the thesis work thus show wavelengths typical to both mesospheric GWs and mesospheric bores.

Dune propagation speeds were not estimated by Palmroth et al., but Grandin et al. estimated the 2016 dune event to have a propagation speed of the order of 202($\pm$27) - 236($\pm$32) m/s. This is significantly higher than the corresponding quantities found both in this thesis work, the Halley climatology study and previously observed mesospheric bores. It was suggested that the high estimated speed could be explained by horizontal winds increasing the observed speed of the dune. Grandin et al. also mentions a significant uncertainty associated with the images used to estimate the speed. The images are citizen observations, taken with cameras pointing towards the horizon, effectively mapping the three-dimensional structure to a 2D image. The images have been used to estimate wavelength and period, which in turn have been used to estimate the propagation speed. It is thus possible that the estimated propagation speed is too large, although it must be deemed unlikely that the dunes in that event have a true propagation speed in the order of typical GWs. It should however be noted that the estimated dune speed is in the range of the speeds estimated for events analysed in this thesis work when correcting for the possibility of waves traveling one wavelength further than calculated during cadence time Δt, which were between 143 m/s and 228 m/s. This might ask the question of whether any of the studies may have such an estimation error.

An especially noticeable point from the 2021 study by Grandin et al. is the large scale of the 2016 dune event. The structures spanned over 1500 km, which is far beyond the observed span of the finger structures, given that the projected airglow images have a field of view of 300 km. The dunes were furthermore observed for at least 4 h, contrary to the observed time spans of the finger structure events, which were between 31 and 68 minutes. GWs are as mentioned unstable in the MLT, making it highly unlikely that a normal GW would show horizontal and time spans as the 2016 dune event. The 1993 and 2001 mesospheric bore events do however show similar time spans of 2 h and 3 h respectively (Taylor et al., 1995; Nielsen et al., 2005). Given that the events were observed using airglow imagers, a spatial span cannot be given, but the large time span of the 2016 dune event might thus argue that it in fact is the auroral manifestation of mesospheric bores, although estimated speeds are especially high. The 2018 dune event studied by Palmroth et al. in 2020 does however show a more similar time span to the finger structures' time span, being observed for around 30 minutes, and furthermore had an observed horizontal span of around 500 km. It can thus be argued that the 2018 dune event may be the manifestation of normal GWs and not mesospheric bores, given the similarity in horizontal and time span, and that no speed is estimated. This would

certainly increase the transferability between dunes and finger structures.

A noticeable feature of the events analysed in the thesis work is that all events are from a span of five days in June 2000. It could be argued that this questions the transferability between the finger structures and dunes. There are however, several factors that made the beginning of June 2000 especially good for observing finger structures. The light contamination was low both from Sun and Moon, as it was close to the solstice and a new moon on June 3rd. This enabled semi-continuous imaging, only interrupted by short intervals where moonlight was too strong. Weather conditions were also suitable, with little cloud cover in the data. These factors increased the amount of usable data significantly, compared to e.g., a random day in March with cloud cover. Moreover, auroral activity was low enough to not contaminate images entirely, but high enough to see finger structures. Auroral activity seemed to be too low at Rothera, which lies at a geomagnetic latitude of approximately 57° S, compared to Halley, which lies at a geomagnetic latitude of approximately 67° S. Data from Rothera acquired at days where the K_p index was deemed to be high ($K_p \geq 4$) was examined, but nearly all the data was unusable due to cloud cover.

One event was found in KHO data from Svalbard, which is at an even higher geomagnetic latitude than Halley (75° N). Due to poor spatial resolution compared to wavelengths, it was not possible to analyse this event in more detail. BAS has quick-look data in the form of day-by-day OH airglow-videos, which give a good impression of visual and auroral conditions. The same kind of quick-look data was not available for KHO data, which may have contributed to why events from KHO were harder to find. Auroral conditions and cloud cover did however seem promising with respect to finding more similar events in KHO data. It is however not sufficient to observe aurora while good visibility to classify it as a finger structure event. GW activity also needs to be at a sufficient level, which seemed to be the case for both Halley and KHO data. The climatological study of short-period mesospheric GWs over Halley during the winters of 2000 and 2001 reported of 221 wave events (Nielsen et al. 2001). A similar study was performed using data from the EISCAT Svalbard Radar from March 2007 to February 2008, and it reported of 244 cases of visible GW signatures (Vlasov et al., 2011).

CHAPTER 5

Conclusion and Further Work

Airglow imager data from Halley and Rothera at Antarctica, as well as KHO at Svalbard was analysed to find events where finger structures in aurora relating to GWs were visible. The aim was to answer two important questions related to the newly discovered dune structures: if the finger structures were GWs illuminated by the aurora, and to find out if the waves could be mesospheric bores. Geographically projected Na and OH airglow images were obtained and contrast stretched to enhance airglow and auroral structures, respectively, and four events showing finger structures relating to GWs were found. One event was found in data from KHO, and three events were found in data from Halley Research Station, June 2000. For the three events found in Halley data, wavelengths, finger structure separations and wave propagation speeds were estimated. The wavelengths seemed to be fairly constant throughout the events, indicating a low auroral influence on the waves. Additionally, wavelengths and finger structure separations were found to be fairly similar. These findings are interpreted as the finger structures being aurorally independent GWs illuminated by the aurora. Wave propagation speeds were found to be significantly lower than typical mesospheric bore speeds, strongly indicating that the waves analysed were GWs. The connection between finger structures and atmospheric waves is in agreement with previous dune literature, suggesting that illuminated atmospheric waves are the cause of the dune structures, and that dunes are not an auroral structure. The fact that the atmospheric waves are ordinary GWs are on the other hand not in agreement with previous dune literature, which has pointed to mesospheric bores. A comparison of parameters from finger structure events analysed in this thesis work and

5.1 Further Work

Further work should first and foremost focus on finding more finger structure events. A more sophisticated study should be conducted, which considers auroral activity, visibility and GW activity. A good starting point would be to find days with a similar K_p-index and visibility as on June 3rd, 4th and 7th 2000. It is probable that such a study would find more events in data from both Halley and KHO imagers, from which there exists several winters worth of data. Airglow data from other locations at similar latitudes to Halley and KHO should also be considered. Finding more events would strengthen the transferability between finger structures and dunes, further support the hypothesis that dunes are not auroral structures and give more knowledge on whether dunes may be GWs.

Furthermore, the possibility of a more advanced analysis and filtering of airglow images should be considered both for events analysed in this thesis work and any future events to be analysed. The possibility of a 2D-Fourier analysis should for example be considered, in addition to a better filtering so that zenith structures do not disappear. Supplementing the airglow data should also be considered. Imaging riometry data as described by Jarvis et al. (2003) for the June 7th 2000 GW event could reduce the troubles associated with light contamination. Temperature profile data could be studied to find out whether a bore-ducting channel is present. O and O_2 airglow images could be studied for Halley and Rothera data to find out whether there exists a symmetric bore.

References

[1] Andrews, D.G. (2010). *An Introduction to Atmospheric Physics.* Cambridge: Cambridge University Press.

[2] Baker, D.J., Romick, G.J. (1976). The rayleigh: interpretation of the unit in terms of column emission rate or apparent radiance expressed in SI units. *Applied Optics*, 15, 1966-1968. https://doi.org/10.1364/AO.15.001966

[3] BAS (2021). *British Antarctic Survey Database.* http://psddb.nerc-bas.ac.uk/data/access/download.php?menu=4&bc=1,4,7,8,9,9&class=100&type=Airglow&site=Halley&year=2000&day=158&month=06

[4] Bernard, R. (1939). The identification and the origin of atmospheric sodium. *The Astrophysical Journal*, 89, 133-135. https://doi.org/10.1086/144028

[5] Chamberlain, J.W. (1961). *Physics of the Aurora and Airglow.* New York: Academic Press.

[6] Chamberlain, J.W. (1995). The Rayleigh: A Photometric Unit for the Aurora and Airglow. *Physics of the Aurora and Airglow*, J.W. Chamberlain (Ed.).

[7] Chapman, S. (1939). Notes on Atmospheric Sodium. *The Astrophysical Journal*, 90, 309-316. https://doi.org/10.1086/144109

[8] Charters, P.E., Macdonald, R.G., Polanyi, J.C. (1971). Formation of Vibrationally Excited OH by the Reaction H + O_3. *Applied Optics*, 10(8), 1747–1754. https://doi.org/10.1364/AO.10.001747

[9] Dewan, E. M. and R. H. Picard (1998), Mesospheric bores, *J. Geophys. Res.*, 103, 6295 – 6305. https://doi.org/10.1029/97JD02498

[10] Egeland, A., Holter, Ø., Omholt, A. (1973). *Cosmical Geophysics*. Oslo: Universitetsforlaget.

[11] Espy, P.J. (2021). Personal communication.

[12] Garcia, F.J., Taylor, M.J., Kelley, M.C. (1997). Two-dimensional spectral analysis of mesospheric airglow image data. *Applied Optics* 36, 7374-7385. https://doi.org/10.1364/AO.36.007374

[13] Hemmer, P.C. (2005). *Kvantemekanikk*. Trondheim: Tapir Akademisk Forlag.

[14] Hocking, W.H. (2001). Personal communication.

[15] Hunten, D.M., Roach, F., Chamberlain, J.W. (1956). A photometric unit for the airglow and aurora. *Journal of Atmospheric and Solar-Terrestrial Physics*, 8, 345-346. https://doi.org/10.1016/0021-9169(56)90111-8

[16] Jarvis, M.J., Hibbins, R.E., Taylor, M.J., and Rosenberg, T.J. (2003). Utilizing riometry to observe gravity waves in the sunlit mesosphere, *Geophys. Res. Lett.*, 30, 1979. https://doi.org/10.1029/2003GL017885

[17] MATLAB. (2020). version 9.9.0 (R2020a). Natick, Massachusetts: The MathWorks Inc.

[18] Meinel, A.B. (1950). OH Emission Bands in the Spectrum of the Night Sky. *The Astrophysical Journal*, 355, 555-564. https://doi.org/10.1086/145321

[19] Nielsen K., Taylor M.J., Hibbins R.E. and Jarvis M.J. (2001). Climatology of short-period mesospheric gravity waves over Halley, Antarctica (76°S, 27°W), *Journal of Atmospheric and Solar-Terrestrial Physics*, 71, 8-9. https://doi.org/10.1016/j.jastp.2009.04.005

[20] Nielsen, K., Taylor, M. J., Stockwell, R. G., and Jarvis, M. J. (2006), An unusual mesospheric bore event observed at high latitudes over Antarctica, *Geophys. Res. Lett.*, 33, L07803. https://doi.org/10.1029/2005GL025649

[21] Palmroth, M., Grandin, M., Helin, M., Koski, P., Oksanen, A., Glad, M. A., et al. (2020). Citizen scientists discover a new auroral form: Dunes provide insight into the upper atmosphere. *AGU Advances*, 1, e2019AV000133. https://doi.org/10.1029/2019AV000133

[22] Partamies, N. (2022). Personal communication.

[23] Plane, J.M.C. (2003). Atmospheric Chemistry of Meteoric Metals. *Chemical Reviews*, 103 (12), 4963-4984. https://doi.org/10.1021/cr0205309

[24] Plane, J.M.C. . Personal communication.

[25] Sivjee, G. G. and Hamwey, R. M. (1987), Temperature and chemistry of the polar mesopause OH, *J. Geophys. Res.*, 92, 4663– 4672. https://doi.org/10.1029/JA092iA05p04663

[26] Slipher V.M. (1929). Emissions in the Spectrum of the Light of the Night Sky. *Publ. Astron. Soc. Pac.*, 41, 262–265.

[27] Størmer, C. (1955). *The Polar Aurora*. Oxford: Clarendon Press.

[28] Taylor, M. J., Turnbull, D. N. and Lowe, R. P. (1995). Spectrometric and imaging measurements of a spectacular gravity wave event observed during the ALOHA-93 Campaign. *Geophys. Res. Lett.*, 22, 2849-2852. https://doi.org/10.1029/95GL02948

[29] Taylor, M.J. (2000). *The Utah-BAS Airglow Imaging Experiment Operation Manual*.

[30] Vlasov, A., K. Kauristie, M. van de Kamp, J.-P. Luntama, and A. Pogoreltsev (2011). A study of Traveling Ionospheric Disturbances and Atmospheric Gravity Waves using EISCAT Svalbard Radar IPY-data. *Ann. Geophys.*, 29, 2101-2116. https://doi.org/10.5194/angeo-29-2101-2011

APPENDIX A

Svalbard Finger Structure Event

Figure A.1 shows airglow images taken at KHO January 3rd 2022 with what seems to be finger structures in the filter 2 image at 08:15 UT. GW structures are simultaneously visible in the filter 6 image. The finger structure separation and GW wavelength was too small to be properly analysed.

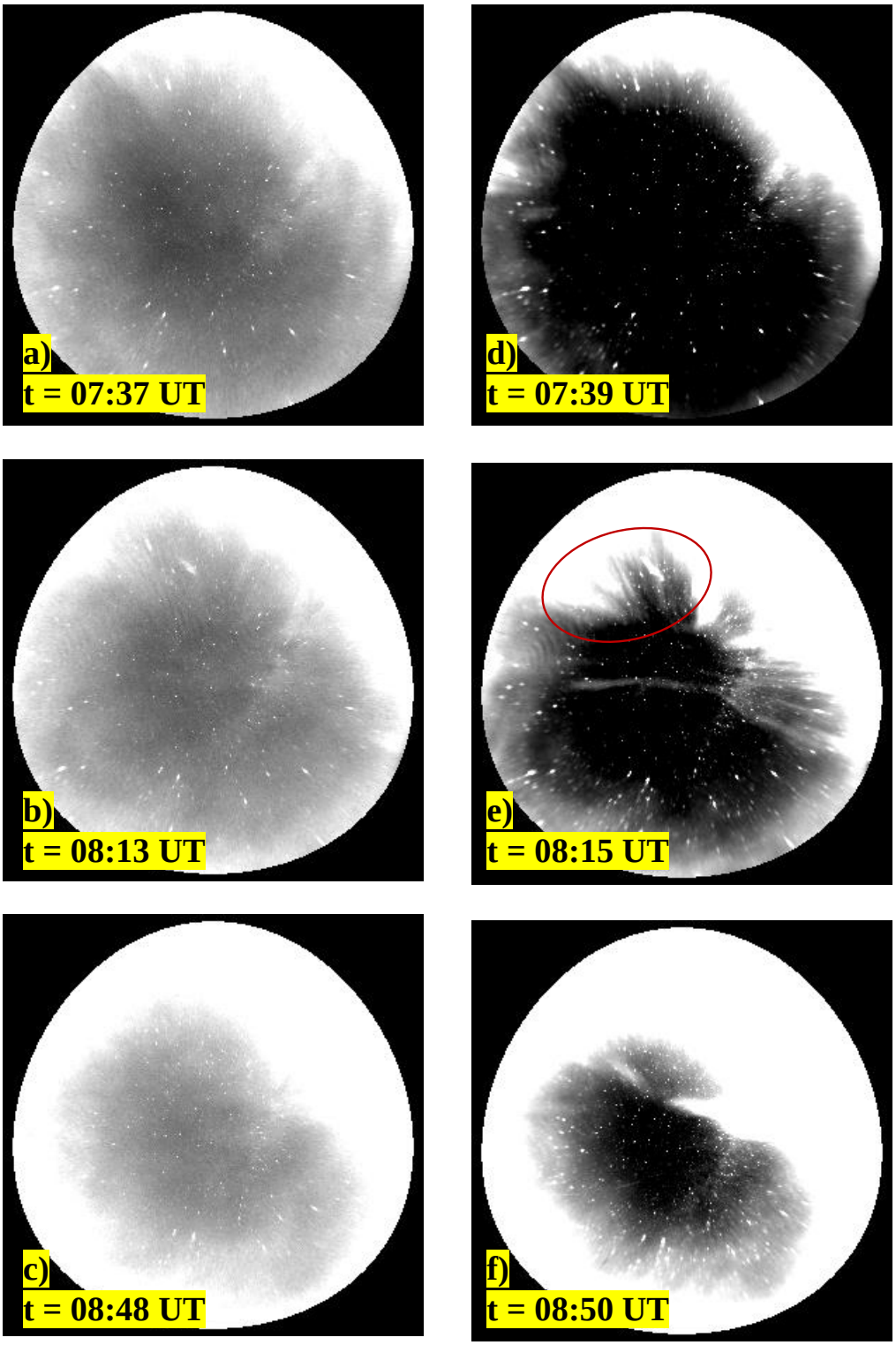

Figure A.1: Contrast stretched airglow images taken at times t, January 3rd 2022. a)-c) are images taken with filter 6 and have contrast stretching parameters $[l, u] = [1260, 2400]$. d)-f) are taken images taken with filter 2 and have contrast stretching parameters $[l, u] = [18455, 25920]$. The finger structures are circled in e).

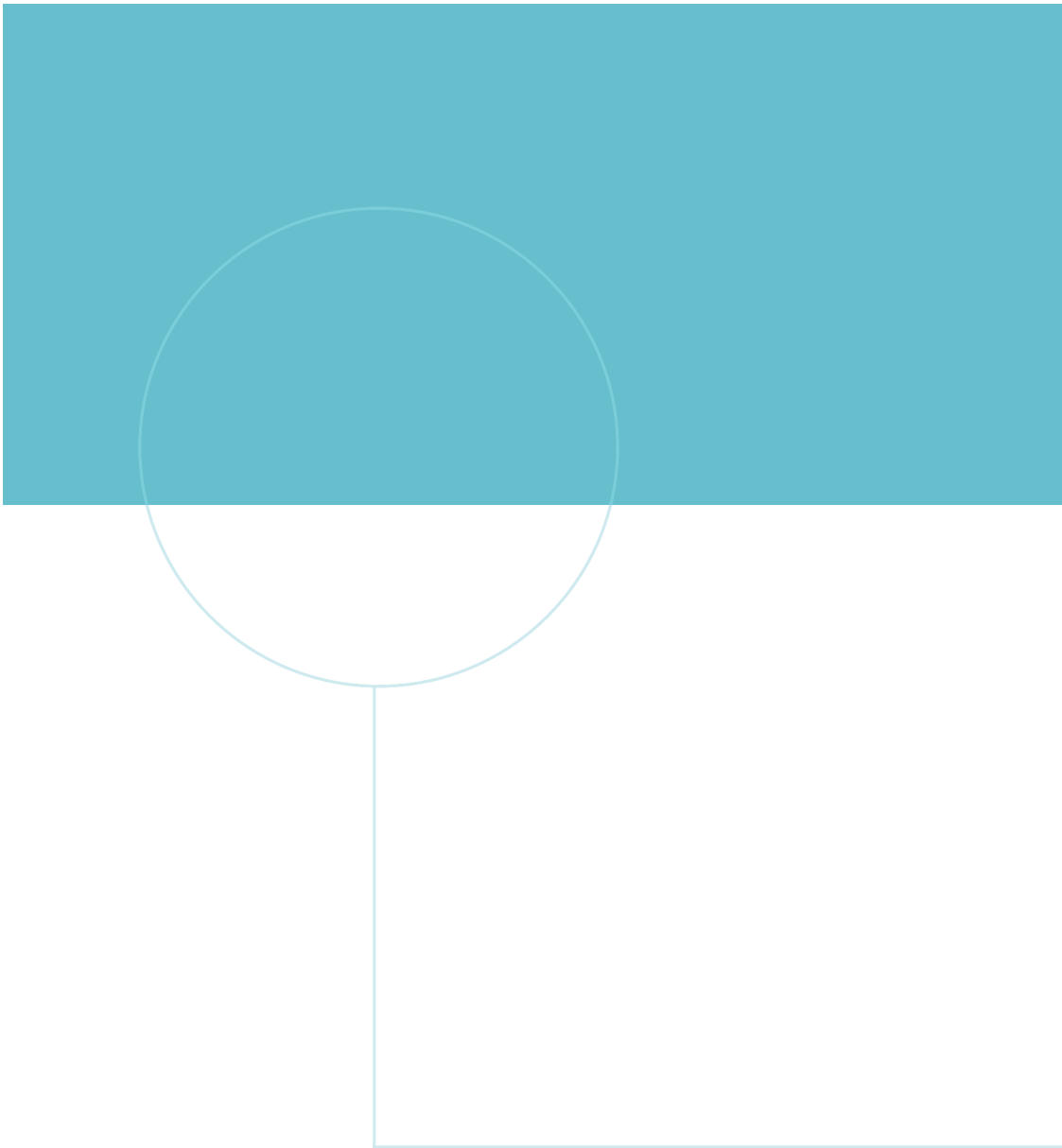

NTNU
Norwegian University of
Science and Technology

UNIS
The University Centre in Svalbard